Numerical Entropy Production for Central Schemes

Gabriella Puppo*

Abstract

In this work a detailed study of the numerical entropy production for both low and high order central schemes is carried out. Our data suggest that the entropy production can be used to signal the presence of shocks. Moreover, once shocked cells have been identified, the spurious entropy production occurring in the remaining cells mimics the behaviour of the local error, and therefore it can be used as an a posteriori error indicator. We also investigate numerically the entropic properties of third and fourth order Central WENO schemes. To our knowledge, this is the first study of the entropic behaviour of such high order schemes.

Key words. Conservation laws, numerical entropy, central difference schemes, high-order accuracy, a posteriori error.

AMS(MOS) subject classification. Primary 65M06; secondary 65M99.

Contents

1 Introduction **2**

2 Numerical entropy production for Lax-Friedrichs and Godunov schemes **3**
2.1 Computing the entropy production for the linear advection equation 4
2.2 Computing the entropy production on a shock 6
2.3 Numerical results 9

3 Numerical entropy production for high order schemes **11**
3.1 The Nessyahu-Tadmor's scheme 13
3.2 The Compact Central WENO scheme 15
3.3 The Central WENO scheme 18

4 Applications **21**
4.1 Are high-order Central WENO schemes entropic? 22
4.2 Entropy production as a discontinuity detector 24
4.3 Entropy production as error indicator 27

*Dipartimento di Matematica, Politecnico di Torino, Corso Duca degli Abruzzi 24, 10129 Torino, Italy; puppo@calvino.polito.it

1 Introduction

We consider the scalar conservation law:

$$u_t + f_x(u) = 0. \tag{1.1}$$

We choose an entropy function $\eta(u)$ and we associate to the conservation law the entropy inequality:

$$\eta_t + \psi_x(u) \le 0, \quad \text{with} \quad \psi'(u) = \eta'(u) f'(u). \tag{1.2}$$

We cover the computational region with control volumes $V_j^n = I_j \times [t^n, t^{n+1}]$, where $t^{n+1} = t^n + \Delta t$, $I_j = [x_j - h/2, x_j + h/2]$ and $x_{j+1} = x_j + h$.

Integrating the conservation law (1.1) over the control volumes V_j^n, we find the finite volume formulation:

$$\frac{1}{h}\int_{I_j} u^{n+1}(x)\, dx = \frac{1}{h}\int_{I_j} u^n(x)\, dx - \lambda \frac{1}{\Delta t}\int_{t^n}^{t^{n+1}} \left[f(u(I_j^+, \tau)) - f(u(I_j^-, \tau)) \right] d\tau. \tag{1.3}$$

here I_j^+ and I_J^- denote the right and left end points of the interval I_j and $u^n(x) = u(x, t^n)$, with $t^n = n\Delta t$. Finally, $\lambda = \Delta t / h$ is the mesh ratio.

Integrating the entropy inequality over the same control volume, we find the finite volume formulation of the entropy inequality:

$$\frac{1}{h}\int_{I_j} \eta(u^{n+1}(x))\, dx - \frac{1}{h}\int_{I_j} \eta(u^n(x))\, dx + \frac{\lambda}{\Delta t}\int_{t^n}^{t^{n+1}} \left[\psi(u(I_j^+, \tau)) - \psi(u(I_j^-, \tau)) \right] d\tau \le 0; \tag{1.4}$$

If the solution is smooth, it is well known that both (1.3) and (1.4) are zero. If a shock crosses the V_j^n control volume, (1.3) is satisfied, but (1.4) will not be zero, instead its sign characterizes the physically relevant unique solution to (1.1).

When the finite volume formulation (1.3) is discretized the corresponding discretized version of (1.4) will not be zero even for smooth flows. We claim that the amount by which (1.4) fails to be zero on smooth flows yields a measure of the local residual of the conservation law.

The present work is concerned with a numerical study of the quantity:

$$S_j^n = \frac{1}{\Delta t}\left\{ \frac{1}{h}\int_{I_j} \eta(u^{n+1}(x))\, dx - \frac{1}{h}\int_{I_j} \eta(u^n(x))\, dx + \frac{\lambda}{\Delta t}\int_{t^n}^{t^{n+1}} \left[\psi(u)|_{I_j^+} - \psi(u)|_{I_j^-} \right] d\tau \right\}, \tag{1.5}$$

which is the density of numerical entropy production in the V_j^n control volume (in the following it will be called entropy production, for short, when no ambiguities arise). The total entropy production of the scheme then is

$$S = \sum_j \sum_n S_j^n\, h\, \Delta t.$$

It is interesting to note that (1.5) contains the same expression for the entropy used in [3] to construct a MUSCL method specifically designed to satisfy all entropy inequalities.

As we will see, central schemes based on staggered grids yield a natural way for the evaluation of S_j^n. Our tests suggest that the knowledge of S_j^n gives valuable information on the regularity of the solution and on the local error. Moreover the sign of S_j^n will give an indication of the entropic properties of the scheme.

There are no results at present on the entropic properties of higher than second order schemes. The data gathered from numerical tests, in this context, can suggest the entropic behaviour of these schemes and give a direction for rigorous analysis. A first result of this work is the conjecture that high order central schemes may be Essentially Entropic, in the sense that spurious positive overshoots in the entropy production are possible, but their amplitude converges to zero, as the grid is refined.

Another application of the numerical entropy production is to grid control.

The research of reliable and rigorous error indicators for hyperbolic systems of conservation laws is still open. In [17] an a posteriori error indicator is proposed, but it relies on a local linearization of the equations.

More in the line of the present work, in [1] an error indicator is proposed, relying on the discrepancies of an entropy variable, for steady Euler flows.

The preliminary results of this work indicate that a new error indicator can be constructed, based on the local numerical production of entropy, for unsteady flows as well. Moreover, this error indicator can be applied to a wide class of numerical schemes, ranging from first to fourth order accurate.

The paper is organized as follows. In §2 we compare the entropy productions for Godunov and for the staggered Lax Friedrichs schemes. For the linear advection equation, the form of the local truncation error is known, and we can compare the information obtained from the numerical entropy production with the expected error. In the following section, we compare the exact entropy production on a shock with the results obtained with Lax Friedrichs and Godunov schemes.

In §3, we evaluate the numerical entropy production for the second order Nessyahu-Tadmor scheme [14]. Next, we compute the entropy production for the Compact-C-WENO third order scheme [12] and for the fourth order Central WENO scheme [10], and we compare the results obtained with these schemes.

In §4 we study quantitatively the behaviour of the entropy production on a few test cases, comparing the results obtained with all schemes considered. First, we study the entropic properties of the third and fourth order CWENO schemes. Next we use the data gathered from all schemes studied to address the issue of the behaviour of the numerical entropy production as a discontinuity detector. Finally we study the possibility of using the entropy production as a local a posteriori error indicator.

We show our results on two simple scalar test problems. This allows to investigate thouroughly the behaviour of the entropy production on several schemes. The preliminary results we obtain on systems of equations, [15] suggest that most phenomena we describe in this work for the scalar case carry on to the more general case of systems of equations.

Acknowledgements

This work was partially supported under MURST project '99 *Approximation of non-coercive problems with applications to continuum mechanics and electromagnetism*, coord. F. Brezzi and GNCS-INDAM project *Numerical methods for hyperbolic and kinetic equations.*

I wish to thank Denise Aregba Driollet, Roberto Natalini and Giovanni Russo for several helpful discussions.

2 Numerical entropy production for Lax-Friedrichs and Godunov schemes

For Godunov scheme we discretize (1.3) on the control volumes $V_j^n = [x_j - \frac{h}{2}, x_j + \frac{h}{2}] \times [t^n, t^{n+1}]$. The cell averages $\{\overline{u}_j^n\}$ obtained from the previous time step are used to reconstruct the solution at the time level t^n as a piecewise constant function:

$$u^n(x) = \sum_j \overline{u}_j^n \chi_{I_j}(x),$$

where χ_{I_j} is the characteristic function of the interval $I_j = [x_j - \frac{h}{2}, x_j + \frac{h}{2}]$, and $\overline{u}_j^n$ denotes the cell average at time t^n:

$$\overline{u}_j^n = \frac{1}{h} \int_{I_j} u^n(x)\, dx.$$

The updated cell-averages are given by:

$$\overline{u}_j^{n+1} = \overline{u}_j^n - \lambda \left[f(u^*_{j+1/2}) - f(u^*_{j-1/2}) \right], \tag{2.1}$$

where $u^*_{j+1/2} = u^*(\overline{u}^n_j, \overline{u}^n_{j+1})$ denotes the solution at $x_{j+1/2}$ of the Riemann problem with initial data $\{\overline{u}^n_j, \overline{u}^n_{j+1}\}$ centered at the cell interface $x = x_{j+1/2} = x_j + h/2$ (for the notation, see [9]), and $\lambda = \Delta t/h$ is the mesh ratio. The scheme is stable if the Riemann problems defined at each cell interface do not interact in the time interval Δt, i.e. for $\lambda \leq 1/\max|f'(u)|$.

The function u^* is not defined if the Riemann problem results in a stationary shock. However, even in that case $f(u^*)$ is well defined, because the Rankine Hugoniot condition $[f] = s[u]$ yields $[f] = 0$, when $s = 0$, where s is the shock speed. For the present context, we need u^* to be well defined, so that we can compute the entropy flux $\psi(u^*)$. Therefore in the following discussion we will assume there are no stationary shocks.

If the function u^* is well defined, Godunov scheme (2.1) yields a natural discretization of the cell entropy inequality (1.4). Since the numerical solution is piecewise constant, $u^n(x)|_{I_j} \equiv \overline{u}^n_j$. Moreover u^* is constant in time during the whole time step. Therefore the integrals in (1.4) can be evaluated exactly. We thus obtain the density of entropy production for Godunov scheme:

$$S^G_j = \frac{1}{\Delta t}\left\{\eta(\overline{u}^{n+1}_j) - \eta(\overline{u}^n_j) + \lambda\left[\psi(u^*_{j+1/2}) - \psi(u^*_{j-1/2})\right]\right\}, \tag{2.2}$$

where from now on we will drop the index n from the left hand side. Note that the numerical entropy flux $\psi_{j+1/2} = \psi(u^*_{j+1/2})$ is consistent with the exact entropy flux.

We now consider the staggered Lax Friedrichs scheme. Again the solution at time t^n is reconstructed as a piecewise constant function:

$$u^n(x) = \sum_j \overline{u}^n_j \chi_{I_j}(x),$$

but now we integrate on the staggered control volumes $V^n_{j+1/2} = [x_j, x_{j+1}] \times [t^n, t^{n+1}]$. Therefore (see [18]):

$$\overline{u}^{n+1}_{j+1/2} = \frac{1}{2}(\overline{u}^n_j + \overline{u}^n_{j+1}) - \frac{1}{h}\int_{t^n}^{t^{n+1}} \left[f(u(x_{j+1},\tau)) - f(u(x_j,\tau))\right]\, d\tau.$$

The solution remains smooth at x_j and x_{j+1}, provided that $\lambda \leq \frac{1}{2}/\max|f'(u)|$. In this case, the integrals of the fluxes can be evaluated with quadrature. Using a first order quadrature formula, we obtain the staggered Lax Friedrichs scheme:

$$\overline{u}^{n+1}_{j+1/2} = \frac{1}{2}(\overline{u}^n_j + \overline{u}^n_{j+1}) - \lambda\left[f(\overline{u}^n_{j+1}) - f(\overline{u}^n_j)\right]. \tag{2.3}$$

The same discretization applied to the cell entropy inequality (1.4) yields the numerical density of entropy production for the staggered Lax Friedrichs scheme:

$$S^{LF}_{j+1/2} = \frac{1}{\Delta t}\left\{\eta(\overline{u}^{n+1}_{j+1/2}) - \frac{1}{2}\left[\eta(\overline{u}^n_{j+1}) + \eta(\overline{u}^n_j)\right] + \lambda\left[\psi(\overline{u}^n_{j+1}) - \psi(\overline{u}^n_j)\right]\right\}. \tag{2.4}$$

2.1 Computing the entropy production for the linear advection equation

The scalar conservation law (1.1) admits an infinite number of entropy functions (in fact any convex function is an admissible entropy, see, for instance [6]). Instead of studying all resulting entropy inequalities, it is enough to consider only the family of Kruzkov's entropy functions [8], which are given by:

$$\eta(u;c) = |u-c| \quad \text{with} \quad \psi(u;c) = \operatorname{sgn}(u-c)(f(u)-f(c)) \quad \forall c \in \mathcal{R}.$$

Kruzkov's entropies however are not practical for the present application, because S_j is automatically zero, in many non trivial cases, unless c is chosen as a function of the local solution. Thus it would be necessary to change c in each cell. Take for example Godunov scheme. Then, from (2.2), the entropy production computed using Kruzkov's entropy is:

$$\begin{aligned} S^G_j(c) &= \tfrac{1}{\Delta t}\left\{|\overline{u}^{n+1}_j - c| - |\overline{u}^n_j - c|\right. \\ &\left. +\lambda\left[\operatorname{sgn}(u^*_{j+1/2}-c)(f(u^*_{j+1/2})-f(c)) - \operatorname{sgn}(u^*_{j-1/2}-c)(f(u^*_{j-1/2})-f(c))\right]\right\}. \end{aligned}$$

Suppose $f'(u) > 0$ and $\overline{u}_{j-1}^n > \overline{u}_j^n$. Then $u^*_{j+1/2} = \overline{u}_j^n$ and $u^*_{j-1/2} = \overline{u}_{j-1}^n$. Moreover, if CFL holds, $\overline{u}_{j-1}^n \geq \overline{u}_j^{n+1} \geq \overline{u}_j^n$. Suppose $c \notin [\overline{u}_j^n, \overline{u}_{j-1}^n]$, then:

$$\operatorname{sgn}(\overline{u}_j^{n+1} - c) = \operatorname{sgn}(\overline{u}_j^n - c) = \operatorname{sgn}(u^*_{j+1/2} - c) = \operatorname{sgn}(u^*_{j-1/2} - c).$$

If we substitute this in the equation for $S_j^G(c)$, together with the expression for $\overline{u}_j^{n+1}$, given by (2.1), we immediately find $S_j^G(c) = 0$. To find a non zero value for $S_j^G(c)$, we must take $c \in [\overline{u}_j^n, \overline{u}_{j-1}^n]$, i.e. it is necessary to change c in each cell. This example illustrates a more general fact. It is easy to see that the same behaviour will occur, whenever c does not belong to the range of the values of $\overline{u}^n$ which are involved in the construction of $\overline{u}_j^{n+1}$, for all the non-oscillatory schemes studied in this work.

In the following discussion and in all the numerical tests therefore we will consider the entropy $\eta(u) = u^2$ which does not yield $S_j \equiv 0$. This choice appears quite often in the literature: the entropy inequality is proven for the particular case $\eta(u) = \frac{1}{2}u^2$ for the schemes in, among others, [14], [5].

We wish to compare the densities of entropy production obtained with the staggered Lax Friedrichs and Godunov schemes. We consider the linear advection equation $u_t + u_x = 0$. In this case, $u^*(u_j, u_{j+1}) = u_j$. The entropy production for Godunov scheme (2.2) for the entropy $\eta(u) = u^2$ becomes:

$$S_j^G = \frac{1}{\Delta t}\left\{(\overline{u}_j^{n+1})^2 - (\overline{u}_j^n)^2 + \lambda\left[(\overline{u}_j^n)^2 - (\overline{u}_{j-1}^n)^2\right]\right\}.$$

Substituting the expression for $\overline{u}_j^{n+1}$ from (2.1) we find:

$$S_j^G = -h(1-\lambda)\left(\frac{\overline{u}_j^n - \overline{u}_{j-1}^n}{h}\right)^2. \tag{2.5}$$

In the linear advection case, it is possible to justify the choice $\eta(u) = u^2$ with the following argument (Denise Aregba-Driollet, private communication).

Consider Kruzkov's entropies for the particular case of the linear advection equation $u_t + u_x = 0$:

$$\eta(u;c) = |u - c| \quad \psi(u;c) = \operatorname{sgn}(u-c)\,(u-c) = |u-c|.$$

For Godunov scheme, we obtain the density of entropy production:

$$S_{j;c}^G = \frac{1}{\Delta t}\left\{|\overline{u}_j^{n+1} - c| - |\overline{u}_j^n - c| + \lambda(|\overline{u}_j^n - c| - |\overline{u}_{j-1}^n - c|)\right\}.$$

Suppose, without loss of generality, that $\overline{u}_j^n \geq \overline{u}_{j-1}^n$. Then $\overline{u}_{j-1}^n \leq \overline{u}_j^{n+1} \leq \overline{u}_j^n$, if CFL holds, and the following four cases are possible:

1) $c \leq \overline{u}_{j-1}^n$ $\quad S_{j;c}^G = 0$

2) $\overline{u}_{j-1}^n \leq c \leq \overline{u}_j^{n+1}$ $\quad S_{j;c}^G = \frac{2\lambda}{\Delta t}(\overline{u}_{j-1}^n - c)$

3) $\overline{u}_j^{n+1} \leq c \leq \overline{u}_j^n$ $\quad S_{j;c}^G = \frac{2}{\Delta t}(1-\lambda)(c - \overline{u}_j^n)$

4) $c \geq \overline{u}_j^n$ $\quad S_{j;c}^G = 0.$

Now let us compute the average Kruzkov's density of entropy production (we suppress the index n):

$$\begin{aligned} < S_{j;c}^G > &= \int_{-\infty}^{+\infty} S_{j;c}^G\, dc = \int_{\overline{u}_{j-1}}^{\overline{u}_j - \lambda(\overline{u}_j - \overline{u}_{j-1})} \tfrac{2\lambda}{\Delta t}(\overline{u}_{j-1} - c) + \int_{\overline{u}_j - \lambda(\overline{u}_j - \overline{u}_{j-1})}^{\overline{u}_j} \tfrac{2}{\Delta t}(1-\lambda)(c - \overline{u}_j) \\ &= -\tfrac{1}{\Delta t}\lambda(1-\lambda)(\overline{u}_j - \overline{u}_{j-1})^2, \end{aligned}$$

which is exactly the expression for S_j^G, obtained before with $\eta(u) = u^2$. Therefore the choice $\eta(u) = u^2$ yields some sort of average density of entropy production, over all Kruzkov's entropies.

We now compute the density of entropy production for the staggered Lax Friedrichs scheme, again for $\eta(u) = u^2$ on the linear advection equation. In order to compare the two schemes, we consider $\Delta t_{LF} = \frac{1}{2}\Delta t$, since the CFL ratio for the staggered Lax Friedrichs scheme is half the corresponding value of Godunov scheme. The mesh width h is the same for the two schemes. We find:

$$S^{LF}_{j-1/2} = \frac{1}{\frac{\Delta t}{2}} \left\{ (\overline{u}^{n+1}_{j-1/2})^2 - \frac{1}{2}\left[(\overline{u}^n_j)^2 + (\overline{u}^n_{j-1})^2\right] + \frac{\Delta t}{2h}\left[(\overline{u}^n_j)^2 - (\overline{u}^n_{j-1})^2\right] \right\}.$$

Substituting $\overline{u}^{n+1}_{j-1/2}$ with the quantity given by the Lax Friedrichs scheme (2.3), we find:

$$S^{LF}_{j-1/2} = -h(1-\lambda)\frac{1+\lambda}{2\lambda}\left(\frac{\overline{u}^n_j - \overline{u}^n_{j-1}}{h}\right)^2. \tag{2.6}$$

Note that in both cases the entropy is negative, provided CFL holds, i.e. $1 - \lambda > 0$.

Remark

If we compute the entropy production for Lax Friedrichs scheme with Kruzkov's entropies, we can follow the same steps we already described for Godunov scheme. In each control volume $V_{j-1/2}$ and for each value of c, we find a corresponding density of entropy production $S^{LF}_{j-1/2;c}$. Again, if we compute the average of $S^{LF}_{j-1/2;c}$ over all c, we easily find $< S^{LF}_{j-1/2;c} >= S^{LF}_{j-1/2}$, where $S^{LF}_{j-1/2}$ is given in (2.6). In this case too therefore the entropy $\eta(u) = u^2$ yields an average density of entropy production over all Kruzkov's entropies.

We now wish to compare the expressions for S^G_j and $S^{LF}_{j-1/2}$ with the local truncation error of these schemes. To this end, we consider smooth flow and we compute the modified equations for Godunov and Lax Friedrichs schemes, see [9], chap. 11.

For Godunov scheme we find the following modified equation:

$$u_t + u_x = \frac{h}{2}(1-\lambda)u_{xx}. \tag{2.7}$$

We now compute the modified equation for the Lax Friedrichs scheme. To compare the two methods, we need to bring the numerical solution to the same time level; thus we apply the Lax Friedrichs scheme twice, obtaining the method:

$$\overline{u}^{n+2}_j = \overline{u}^n_j - \lambda(\overline{u}^n_{j+1} - \overline{u}^n_{j-1}) + (\frac{1}{4} + \lambda^2)(\overline{u}^n_{j+1} - 2\overline{u}^n_j + \overline{u}^n_{j-1}).$$

We compute the modified equation for this scheme, obtaining:

$$u_t + u_x = \frac{h}{2}(1-\lambda)\frac{1+\lambda}{2\lambda}u_{xx} \tag{2.8}$$

The similarities between the density of entropy production and the leading term in the truncation error (appearing on the Right Hand Side of the modified equations) are indeed striking. In particular, the ratio between the densities of entropy production for the two schemes is the same as the ratio of the respective numerical viscosities.

2.2 Computing the entropy production on a shock

We now compute the entropy production on a shock separating two constant states, comparing the exact result with the numerical entropy production due to Godunov and Lax Friedrichs schemes.

We consider Burger's equation

$$u_t + \left(\frac{1}{2}u^2\right)_x = 0$$

with initial condition:

$$u(x,0) = \begin{cases} u_L & x < x_0 \\ u_R & x > x_0. \end{cases}$$

If $u_L > u_R$, the exact solution is a shock, travelling with speed $s = \frac{1}{2}(u_L + u_R)$. Suppose the shock is initially located in the interval $I_{j+1/2} = [x_j, x_{j+1}]$, i.e. $x_j < x_0 < x_{j+1}$. Suppose moreover that the shock does not leave the control volume $V_{j+1/2} = I_{j+1/2} \times [0, \Delta t]$ in the time Δt.

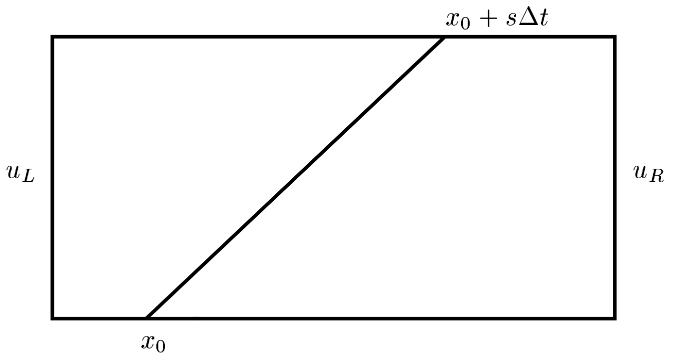

The exact density of entropy production in the cell containing the shock can be easily computed. Let $S(u_L, u_R)$ be the exact density of entropy production due to a shock between the two states u_L and u_R. Consider again $\eta(u) = u^2$. Then $\psi(u) = \frac{2}{3}u^3$, for Burger's equation, and we have:

$$\begin{aligned} S(u_L, u_R) &= \tfrac{1}{\Delta t} \left\{ \tfrac{1}{h} \left[u_L^2(x_0 + s\Delta t - x_j) + u_R^2(x_{j+1} - x_0 - s\Delta t) \right] \right. \\ &\quad \left. - \tfrac{1}{h} \left[u_L^2(x_0 - x_j) + u_R^2(x_{j+1} - x_0) \right] + \tfrac{\Delta t}{h} \left(\tfrac{2}{3}u_R^3 - \tfrac{2}{3}u_L^3 \right) \right\} \\ &= \tfrac{1}{h} \left[(u_L^2 - u_R^2)s + \tfrac{2}{3}(u_R^3 - u_L^3) \right]. \end{aligned}$$

Substitute $s = \frac{1}{2}(u_L + u_R)$; after rearranging, we find:

$$S(u_L, u_R) = -\frac{1}{6h}(u_L - u_R)^3, \tag{2.9}$$

where of course $S(u_L, u_R) < 0$ if $u_L > u_R$, see also [9]. The total amount of entropy dissipated on the shock therefore is

$$\mathcal{S} = -\frac{1}{6}(u_L - u_R)^3. \tag{2.10}$$

The same result holds if the shock crosses the cell wall in the time Δt. In this case, the total entropy production, obtained summing the densities of entropy production over all cells crossed by the shock and multiplying by h, is still given by (2.10).

Usually, numerical schemes spread a shock over more than one cell, creating at least one intermediate state u_C.

With the same technique, we can compute the total density of entropy production resulting from this configuration with two shocks. We find:

$$\begin{aligned} S_C &= S(u_L, u_C) + S(u_C, u_R) \\ &= -\tfrac{1}{6h}(u_L - u_C)^3 - \tfrac{1}{6h}(u_C - u_R)^3. \end{aligned}$$

It can be easily shown that:

$$|S(u_L, u_R)| > |S_C|,$$

provided that the profile is monotone, i.e. $u_L > u_C > u_R$. In fact:

$$S(u_L, u_R) = S(u_L, u_C) + S(u_C, u_R) - \frac{1}{2h}(u_L - u_C)(u_C - u_R)(u_L - u_R).$$

Therefore, the entropy production diminishes (in absolute value) as the profile is spread across the cells. Since the values of u at the spurious intermediate states do not seem to depend on h (see for instance Fig. (3.5)), the numerical entropy production on a shock due to a particular scheme will not converge to the exact entropy production even as $h \to 0$. In fact, as the numerical scheme creates an intermediate state u_C, the term $(u_L - u_C)(u_C - u_R)(u_L - u_R)$ does not converge to zero as $h \to 0$. As we will see below however, this is not the only source of error in the numerical entropy dissipated on a shock.

Let us now compute the densities of entropy production obtained with Godunov and Lax Friedrichs schemes on a shock separating the two states $u_L > u_R$.

Consider the initial data:

$$u_i^n = \begin{cases} u_L & i \le j \\ u_R & i > j \end{cases}$$

Suppose that $s > 0$. Then the solution obtained with Godunov scheme after one time step is:

$$u_i^{n+1} = \begin{cases} u_L & i \le j \\ u_R - \frac{\lambda}{2}(u_R^2 - u_L^2) & i = j+1 \\ u_R & i > j+1. \end{cases}$$

We find that there is only one cell where the density of entropy production is non zero, namely for $i = j+1$. On this cell, for $\eta(u) = u^2$, we find:

$$\begin{aligned} S^G &= \frac{1}{\Delta t}\left\{(u_{j+1}^{n+1})^2 - (u_{j+1}^n)^2 + \frac{2}{3}\lambda\left[(u_{j+3/2}^*)^2 - (u_{j+1/2}^*)^2\right]\right\} \\ &= \frac{1}{\Delta t}\left\{\left[u_R - \frac{\lambda}{2}(u_R^2 - u_L^2)\right]^2 - u_R^2 + \frac{2}{3}\lambda\left[u_R^3 - u_L^3\right]\right\}. \end{aligned}$$

We add and subtract the exact entropy production $S(u_L, u_R)$. After rearranging, we finally find:

$$S^G = S(u_L, u_R) - \frac{s}{h}(u_L - u_R)^2(1 - \lambda s). \tag{2.11}$$

Since $s > 0$ in this example, we see that Godunov scheme provides an extra entropy dissipation with respect to the exact solution, if CFL is satisfied.

We now compute the entropy production for the staggered Lax Friedrichs scheme. Here we find a non zero entropy production only in the cell centered at $x_{j+1/2}$, where:

$$S^{LF} = \frac{1}{\Delta t_{LF}}\left\{(u_{j+1/2}^{n+1})^2 - \frac{1}{2}\left(u_L^2 + u_R^2\right) + \frac{2}{3}\lambda_{LF}(u_R^3 - u_L^3)\right\},$$

where Δt_{LF} and λ_{LF} are the time step and mesh ratio for Lax Friedrichs scheme and:

$$u_{j+1/2}^{n+1} = \frac{1}{2}(u_L + u_R) - \frac{\lambda_{LF}}{2}(u_R^2 - u_L^2).$$

Therefore:

$$S^{LF} = -\frac{1}{6h}(u_L - u_R)^3 - \frac{1}{\Delta t_{LF}}(u_L - u_R)^2\left[\frac{1}{4} - \frac{\lambda_{LF}^2}{4}(u_L + u_R)^2\right].$$

Again, we have an extra amount of entropy production with respect to the exact solution.

To compare S^{LF} and S^G, we substitute, as in the previous section, $\lambda_{LF} = \frac{1}{2}\lambda$. This yields:

$$\begin{aligned} S^G &= S(u_L, u_R) - hs\left(\frac{u_L - u_R}{h}\right)^2(1 - \lambda s) \\ S^{LF} &= S(u_L, u_R) - hs\left(\frac{u_L - u_R}{h}\right)^2(1 - \lambda s)\frac{1 + \lambda s}{2\lambda s}. \end{aligned} \tag{2.12}$$

In both cases, the numerical density of entropy production does not converge to $S(u_L, u_R)$ as $h \to 0$. The situation will be farther complicated in the following time steps, when the shock will be spread on a few cells. On a shock therefore we have two competing phenomena: on the one hand the numerical scheme tends to dissipate more entropy on a given shock than the exact solution. On the other hand, the creation of intermediate states tends to diminish the amount of entropy dissipated on the shock.

However in the cells containing shocks we are not interested in evaluating the local error, which does not go to zero. We are mainly interested in knowing where the shock occurs. And the entropy production contains this information, because for both schemes, as in the exact case, $S \simeq \frac{1}{h}$ in shocked cells. The numerical tests will show that this behaviour persists in the following time steps and for higher order schemes.

Finally we wish to stress the similarity with the linear case. For linear advection infact $S(u_L, u_R) = 0$, and, in the case $u_t + u_x = 0$ studied in the previous section, $s = 1$. Therefore we obtain the same expressions we have already computed in (2.5) and (2.6).

2.3 Numerical results

All schemes have been tested on the same simple test problems. The tests were chosen in order to study the behaviour of the entropy production on a smooth transition, a shock, a contact discontinuity, and a transition with a jump in the first derivative, as an example of a non smooth solution. The two test problems considered are described below.

Test #1
Burger equation:

$$\begin{aligned} &u_t + (\tfrac{1}{2}u^2)_x = 0 \quad \text{on} \quad (-1,1) \\ &u(x,t=0) = 1 + \tfrac{1}{2}\sin(\pi x) \end{aligned}$$

with periodic boundary conditions.

This IVP develops a shock at $T_s = 2/\pi$. The numerical solution is sampled at $T = 0.5 < T_s$ to illustrate the results on a non linear smooth flow. At $T = 1.5$ this test illustrates the behaviour of the entropy production after shock formation.

Test #2
Linear advection:

$$\begin{aligned} &u_t + u_x = 0 \quad \text{on} \quad (-1,1) \\ &u(x,t=0) = \begin{cases} \cos(\frac{\pi}{2}x) & -1 \le x \le 0 \\ \sin(\pi x) & 0 < x \le 1 \end{cases} \end{aligned}$$

with periodic boundary conditions.

The initial data contain a discontinuity and an angular point. Therefore this test describes the behaviour of the entropy indicator on a contact wave and on a region of non-smooth flow.

The results for Test #1 appear in Fig. 2.1 for the case $T = 0.5$ and in Fig. 2.2 for $T = 1.5$. The CFL number is $\lambda = 0.9/\max|f'(u)|$. For Lax Friedrichs scheme: $\Delta t = \frac{1}{2}\lambda h$. The first row of Fig. 2.1 shows the two numerical solutions, superposed. Each column corresponds to a grid size. Here N is the number of grid points per unit length. In the second and third rows we find the density of entropy production for the two schemes.

The two solutions are almost indistinguishable, because, for $\lambda = 0.9$, the two corresponding coefficients of numerical viscosity are almost the same: $\nu_G = 0.05h$ and $\nu_{LF} = 0.052\bar{7}h$. It is also apparent that the entropy production approximately halves as the number of grid points is doubled. Moreover, as expected, the staggered Lax Friedrichs scheme is slightly more diffusive than Godunov and in fact the entropy production is slightly larger for Lax Friedrichs scheme.

Fig. 2.2 shows the results for Test #1 after shock formation. Here we note that for both schemes the entropy production on the shock approximately doubles as the grid is refined, as expected from the analysis in §2.2. This behaviour is markedly different from the one we noticed for smooth flows and it permits to single out shocks from the rest of the flow.

In Fig. 2.3 we show the results obtained on the contact discontinuity of Test #2 for several grid sizes. As the grid is fine enough to resolve it, the contact wave is characterized by a peak in the entropy production. The amplitude of this spurious peak grows slowly under grid refinement, see also Table 4.6. From the data in Table 4.6 for both first order schemes, we see that $S_j \simeq h^{-1/5}$, since on the contact discontinuity the peak in the entropy production approximately doubles after 5 grid refinements.

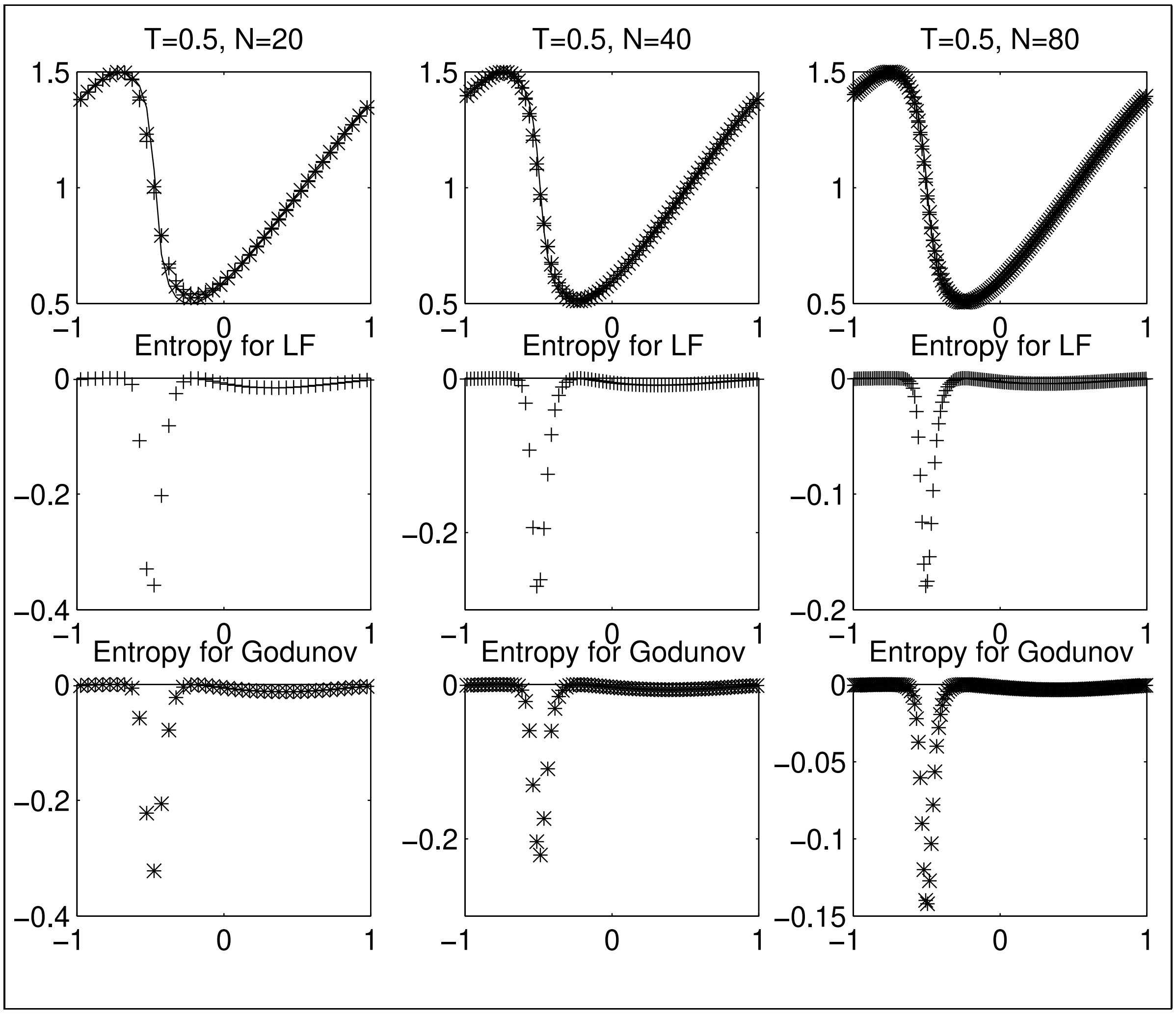

Figure 2.1: Burger's equation. Solution at $T = 0.5$. Comparison between the entropy production of Lax Friedrichs (+) and Godunov (*) schemes on a smooth flow. $\lambda = 0.66$ for Godunov, while Lax Friedrichs has $\lambda = 0.33$.

From §2.2 we know that:

$$S_j \simeq \frac{(\overline{u}_j - \overline{u}_{j-1})^2}{h} \simeq \frac{1}{h^{1/5}}.$$

Let Δ_h be the average jump between neighboring cells in the contact discontinuity on the grid h. Then

$$\Delta_h \simeq (\overline{u}_j - \overline{u}_{j-1}) \simeq h^{2/5}.$$

Now let N_h be the number of points on which the transition is spread on the grid h. Then $N_h \Delta_h$ is of order 1.

We can now estimate the total amount S_h of entropy dissipated on the contact discontinuity by the two first order schemes:

$$S_h = \sum_{N_h} S_j\, h \simeq N_h \frac{\Delta_h^2}{h}\, h \simeq h^{2/5}.$$

We see therefore that the total amount of spurious entropy production dissipated on the linear discontinuity goes to zero as $h \to 0$. More data would be necessary to estimate the actual rate with which $S_h \to 0$. The data in Table 4.6 suggest a rate of convergence of order $h^{2/5}$.

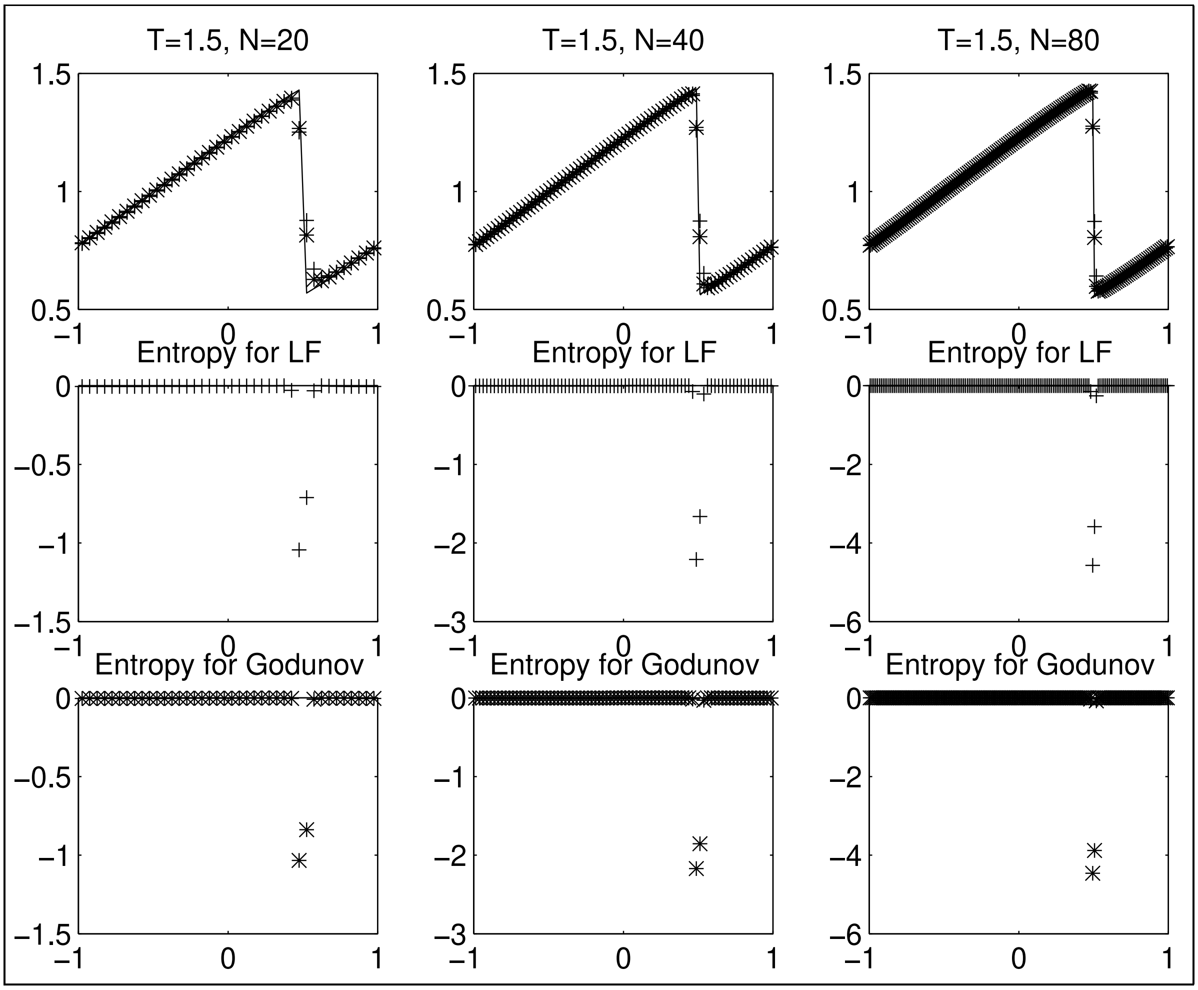

Figure 2.2: Burger's equation. Solution at $T = 1.5$. Comparison between the entropy production of Lax Friedrichs (+) and Godunov (*) scheme on a shock. $\lambda = 0.66$ for Godunov, while Lax Friedrichs has $\lambda = 0.33$.

The amplitude of the peak of spurious entropy production on the angular point goes to zero with an order which is probably slightly slower than h, see also Fig. 4.1.

3 Numerical entropy production for high order schemes

In this section we define the density of entropy production for some high order central schemes, see [18] for a review on central schemes. In particular, we start with the second order Nessyahu-Tadmor's scheme [14], we continue with the third order Compact Central WENO scheme (C-CWENO) [12], and we end with the fourth order Central WENO scheme (CWENO-4) [10]. In the next subsections we first briefly describe each scheme for completeness, and then we define and study the corresponding entropy production in each case.

All schemes in this section are based on a piecewise polynomial reconstruction of degree d:

$$u^n(x) = \sum_j R_j^d(x)\chi_{I_j}(x),$$

where all polynomials R_j^d are obtained from the cell averages at time t^n.

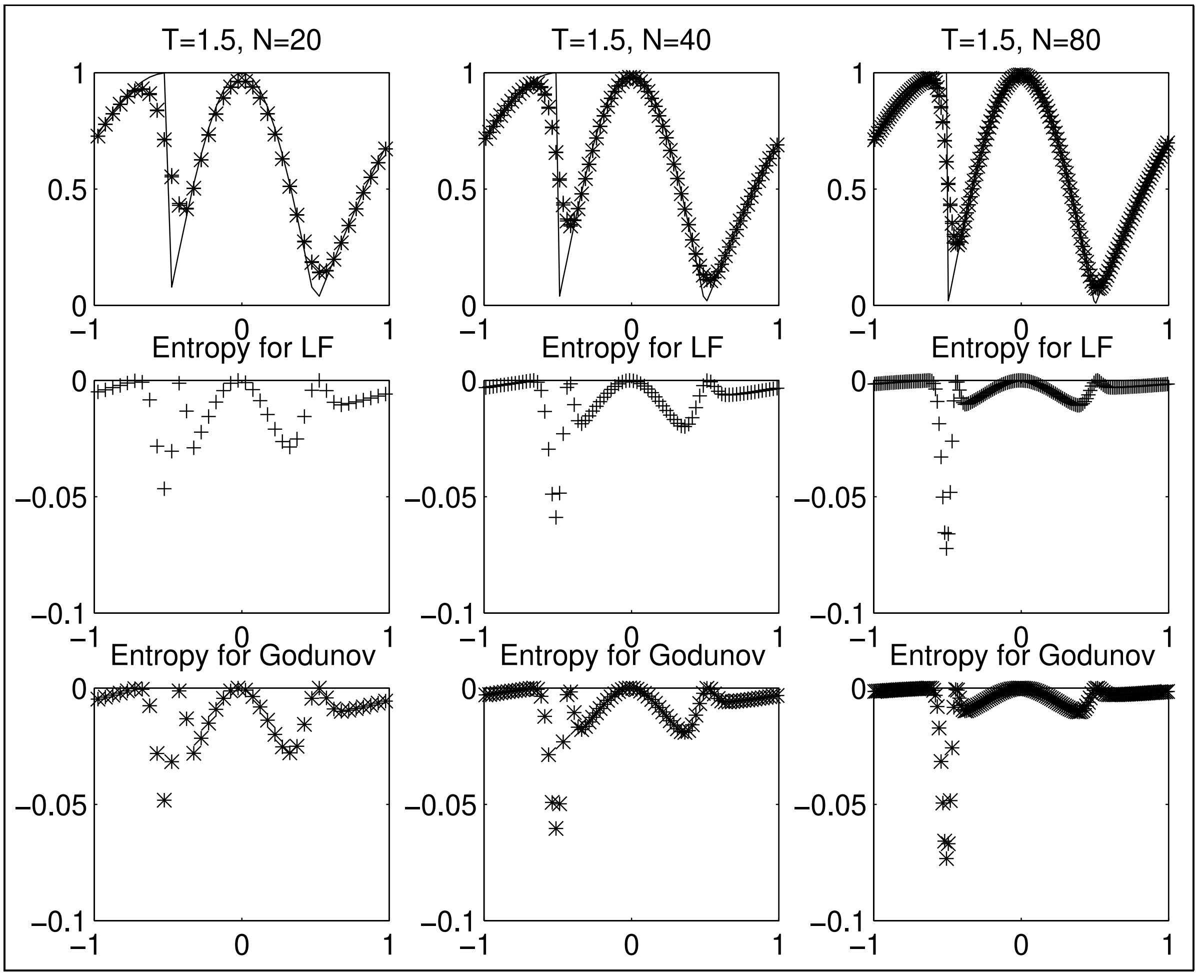

Figure 2.3: Linear advection. Solution at $T = 1.5$. Comparison between the entropy production of Lax Friedrichs (+) and Godunov (*) scheme on a contact wave. $\lambda = 0.9$ for Godunov, while Lax Friedrichs has $\lambda = 0.45$.

As in the staggered Lax Friedrichs scheme, the equation is integrated on the staggered control volume $V^n_{j+1/2}$, and the finite volume formulation for these schemes becomes:

$$\overline{u}^{n+1}_{j+1/2} = \frac{1}{h}\int_{x_j}^{x_{j+1}} u^n(x)\,dx - \frac{1}{h}\int_{t^n}^{t^{n+1}} \left[f(u(x_{j+1},t)) - f(u(x_j,t))\right]\,dt. \tag{3.1}$$

The advantage of this approach is that the discontinuities in the initial data, located at the end points of the cells, $x_{j+1/2}$, now lie in the middle of the control volumes. Therefore the waves resulting from the interaction of the data $u^n(x^-_{j+1/2})$ and $u^n(x^+_{j+1/2})$ do not reach the boundaries of the control volume if Δt is small enough. More precisely, if Δt is chosen in order to satisfy the more restrictive CFL condition:

$$\Delta t \le \frac{h}{2}\frac{1}{\max|f'(u)|}, \tag{3.2}$$

then we can assume that the solution u remains smooth at x_j and x_{j+1} for $t^n \le t \le t^{n+1}$, and the time integrals in (3.1) can be computed with quadrature.

For these schemes the density of entropy production will also be evaluated on the staggered control volumes.

3.1 The Nessyahu-Tadmor's scheme

The central second order Nessyahu-Tadmor's scheme was first described and analyzed in [14].

In this scheme the reconstruction is piecewise linear:

$$u^n(x) = \sum_j R_j^1(x)\chi_j(x) = \sum_j \left(\overline{u}_j^n + u_j' \frac{x - x_j}{h} \right) \chi_{I_j}(x),$$

where $\frac{1}{h}u_j'$ is a non-oscillatory approximation of the first derivative:

$$u_j' = \mathrm{MinMod}\left(\theta(\overline{u}_{j+1}^n - \overline{u}_j^n), \frac{\overline{u}_{j+1}^n - \overline{u}_{j-1}^n}{2}, \theta(\overline{u}_j^n - \overline{u}_{j-1}^n) \right), \tag{3.3}$$

and:

$$\mathrm{MinMod}(a, b, c) = \begin{cases} \mathrm{sgn}(a)\min(|a|, |b|, |c|) & \text{if } \mathrm{sgn}\, a = \mathrm{sgn}\, b = \mathrm{sgn}\, c \\ 0 & \text{otherwise.} \end{cases}$$

For $\theta = 1$, (3.3) reduces to the usual MinMod; for $\theta > 1$, the limiter is less diffusive, because the central derivative $(\overline{u}_{j+1}^n - \overline{u}_{j-1}^n)/2$ can be selected.

As in the staggered Lax Friedrichs scheme, the conservation law is integrated on the staggered control volume $V_{j+1/2}^n = [x_j, x_{j+1}] \times [t^n, t^{n+1}]$, yielding equation (3.1).

If Δt satisfies the CFL condition (3.2), the integral of the fluxes in (3.1) can be evaluated by quadrature. The quadrature rule needs to be more precise than for Lax Friedrichs scheme. For the second order scheme, the mid-point rule is used:

$$\int_{t^n}^{t^{n+1}} f(u(x_j, t^n))\, dt = \Delta t\, f\left(u(x_j, t^n + \frac{\Delta t}{2}) \right) + O(\Delta t)^3.$$

Since the solution is smooth at x_j if the CFL condition above is satisfied, the value of u at the intermediate time $t^n + \frac{\Delta t}{2}$ can be predicted with Taylor's expansion:

$$u(x_j, t^n + \frac{\Delta t}{2}) = u(x_j, t^n) + \frac{\Delta t}{2} u_t + O(\Delta t)^2 = \overline{u}_j^n - \frac{\lambda}{2} f'(\overline{u}_j^n) u_j' + O(\Delta t)^2.$$

The scheme can be written as a two step method. First, compute the approximate slopes as in (3.3), next evaluate:

$$u_j^{n+1/2} = \overline{u}_j^n - \frac{\lambda}{2} f'(\overline{u}_j^n) u_j' \tag{3.4}$$

$$\overline{u}_{j+1/2}^{n+1} = \frac{1}{2}(\overline{u}_{j+1}^n + \overline{u}_j^n) - \frac{1}{8}(u_{j+1}' - u_j') - \lambda \left[f(u_{j+1}^{n+1/2}) - f(u_j^{n+1/2}) \right], \tag{3.5}$$

where the first two terms on the Right Hand Side are the result of the exact evaluation of $\int_{x_j}^{x_{j+1}} u^n(x)\, dx$.

In [14] it is proven that the scheme (3.5) is TVD for $1 \le \theta \le 4$ under the more restrictive CFL condition:

$$\lambda \max |f'(u)| \le \beta \qquad \beta \le \frac{1}{2\theta} \left(\sqrt{4 + 4\theta - \theta^2} - 2 \right),$$

and that the scheme satisfies a cell entropy inequality for the entropy $\eta(u) = u^2/2$ for $0 < \theta \le 1$. However the Authors claim that this CFL condition is not sharp, and they suggest to use the value $\beta = 1/2$, which is the value we will use in the numerical tests. This value infact will yield stable and oscillation free solutions in all our tests even on fine grids.

To compute the entropy production, we evaluate the updated reconstruction at the end of each time step:

$$u_{j+1/2}^{n+1}(x) = \overline{u}_{j+1/2}^{n+1} + u_{j+1/2}' \frac{x - x_{j+1/2}}{h}.$$

Using the same discretization of the scheme, we compute the density of entropy production on the staggered control volume:

$$\begin{aligned} S^{NT}_{j+1/2} \;=\; & \frac{1}{\Delta t}\left\{ \frac{1}{h}\int_{x_j}^{x_{j+1}} \eta\left(u^{n+1}_{j+1/2}(x)\right) - \frac{1}{h}\left[\int_{x_j}^{x_{j+1/2}} \eta\left(u^n_j(x)\right) + \int_{x_{j+1/2}}^{x_{j+1}} \eta\left(u^n_{j+1}(x)\right)\right] + \right. \\ & \left. \lambda\left[\psi\left(u^{n+1/2}_{j+1}\right) - \psi\left(u^{n+1/2}_j\right)\right] \right\}, \end{aligned} \tag{3.6}$$

where the space integrals can be computed exactly, once $\eta(u)$ is specified. Note that all quantities involved in the evaluation of $S^{NT}_{j+1/2}$ need to be computed in order to apply the scheme, so no extra function evaluations are necessary to compute $S^{NT}_{j+1/2}$.

In the numerical tests, we compare Nessyahu-Tadmor's scheme with $\theta = 1$ and $\theta = 2$ (denoted with a $+$ and a $*$ respectively, in the figures) in the evaluation of the approximate slopes.

Fig. 3.1 shows the results obtained for Burger's equation before shock formation (see Test #1 of §2.3, T=0.5)

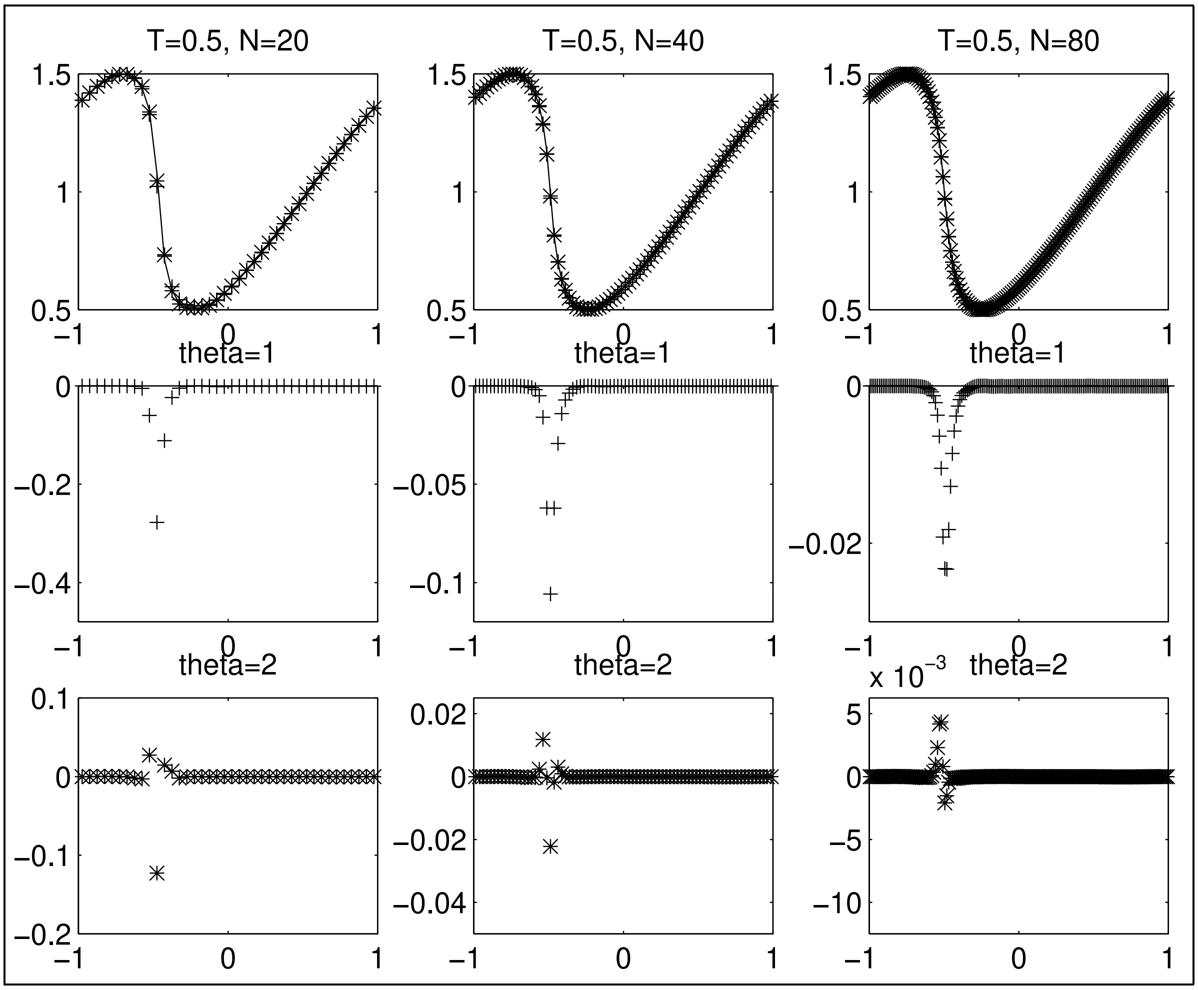

Figure 3.1: Burger's equation. Solution at $T = 0.5$, $\lambda = 0.33$. Nessyahu-Tadmor's scheme with two different limiters on a smooth flow.

We note that the two numerical solutions are very close. Still, there is more spurious entropy production for $\theta = 1$ than for $\theta = 2$, corresponding to a higher resolution in the second case. The spurious entropy production decreases roughly as h^2 as the grid is refined, see also Table 4.7 for more quantitative results. It is also apparent that the numerical solution is entropic for $\theta = 1$, while there are some positive overshoots for $\theta = 2$, the amplitude of which decreases fast as the grid is refined.

The results after shock formation are shown in Fig. 3.2. In this case, the results obtained with the two limiters are almost indistinguishable, and the amplitude of the entropy peak goes roughly as $\frac{1}{h}$ as the grid is refined, as we observed for the first order schemes (see § 2.3 and Fig 2.2).

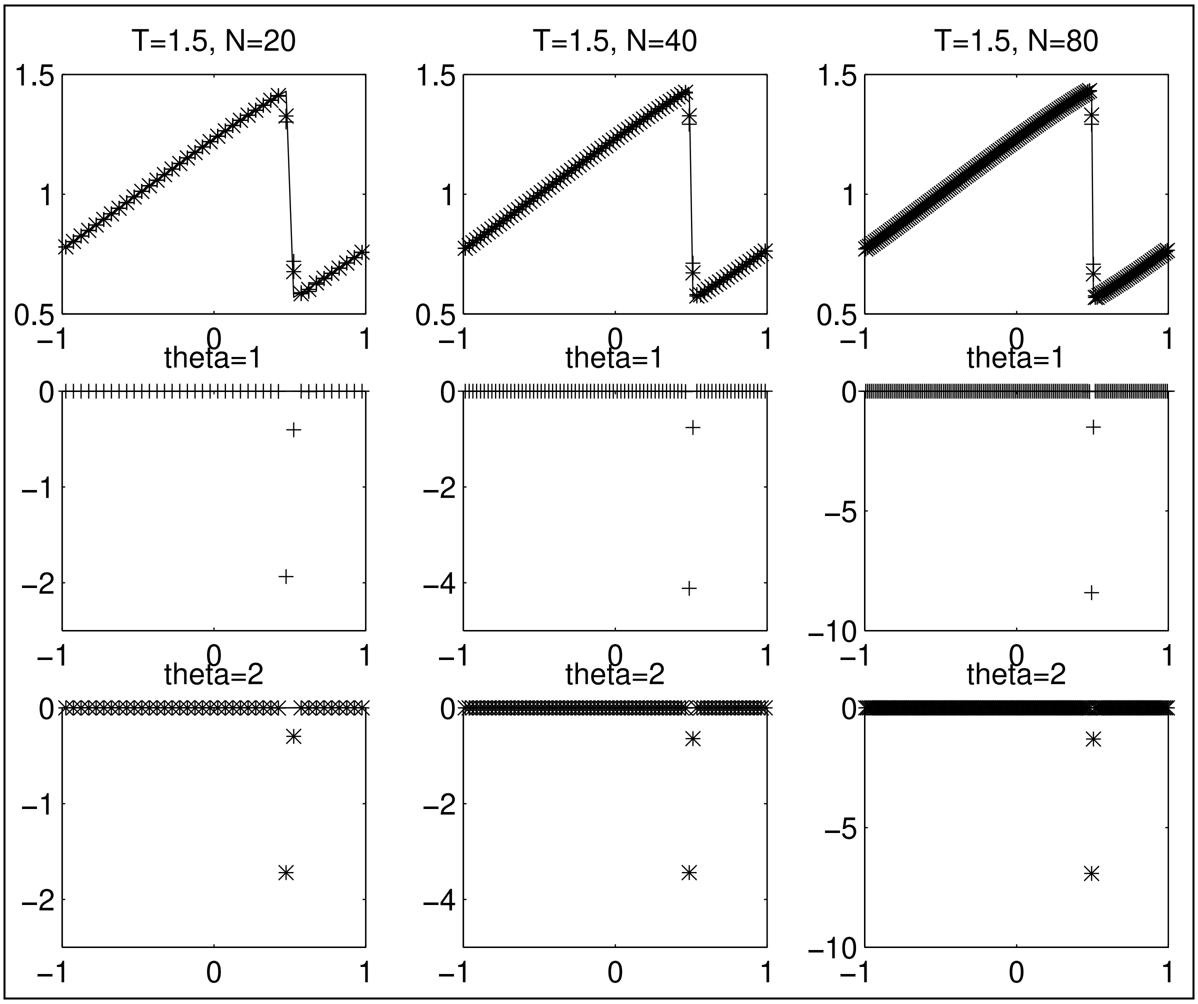

Figure 3.2: Burger's equation. Solution at $T = 1.5$, $\lambda = 0.33$. Nessyahu-Tadmor's scheme with two different limiters on a shock.

Finally Fig. 3.3 shows the entropy production on a contact discontinuity. We note that the numerical solution corresponding to $\theta = 1$ is slightly more diffusive and it yields a larger spurious entropy production. In both cases, the spurious entropy production on the contact wave grows very slowly as the grid is refined, see also Table 4.6. The angular point generates a small amount of spurious entropy and is well resolved for both values of θ, see also Fig. 4.1.

3.2 The Compact Central WENO scheme

The Compact Central WENO scheme (CCW-3) was first described in [12]. As the fourth order Central WENO scheme which will be described next, it is based on adaptating the WENO reconstruction proposed in [7] to the central framework.

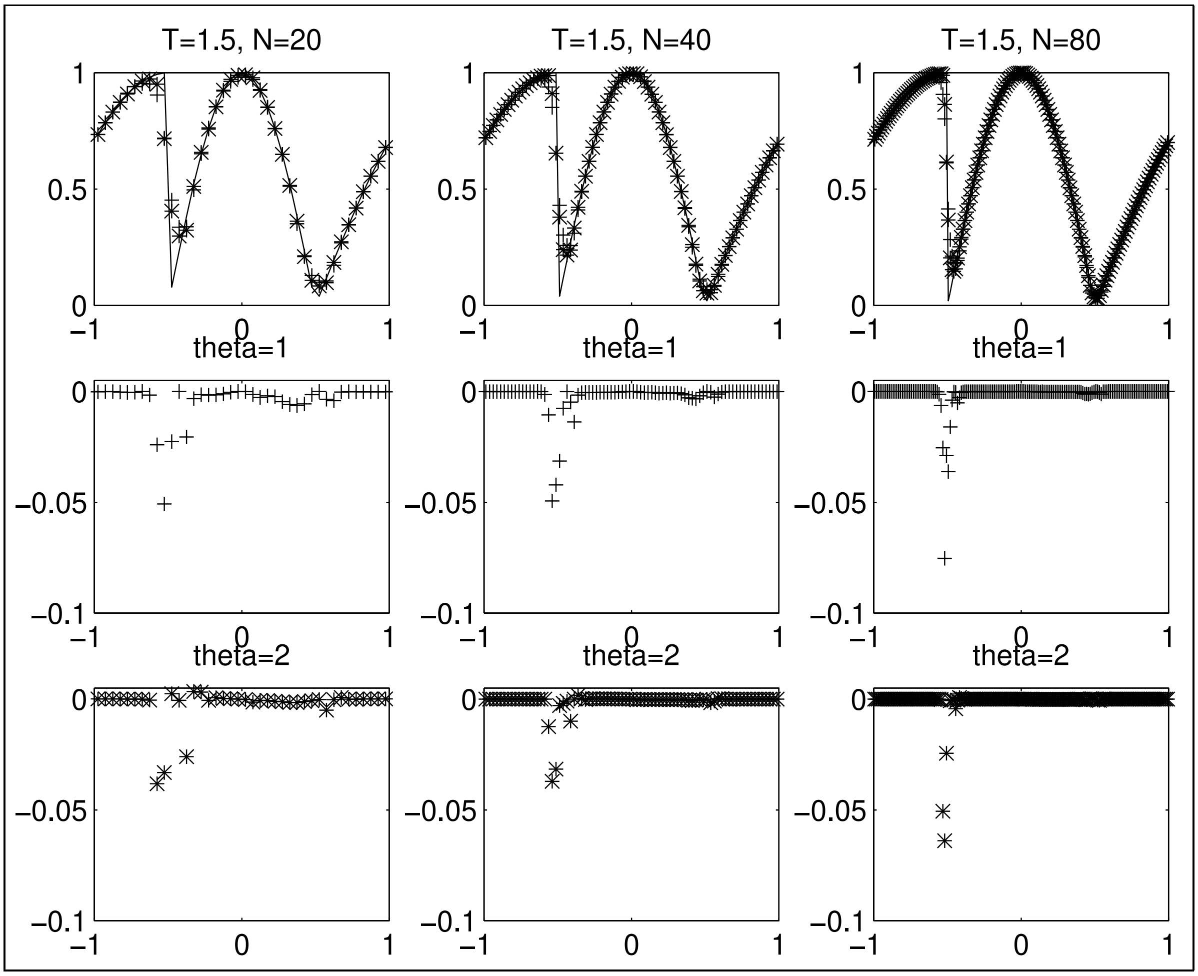

Figure 3.3: Linear advection. Solution at $T = 1.5$, $\lambda = 0.45$. Nessyahu-Tadmor's scheme with two different limiters on a contact wave.

We consider the piecewise parabolic reconstruction:

$$u^n(x) = \sum_j R_j^2(x)\chi_{I_j}(x).$$

The parabola $R_j^2(x)$ is based on the superposition of three polynomials: two one sided linear functions, namely:

$$P^1_{j,-1}(x) = \overline{u}_{j-1} + \tfrac{\overline{u}_j - \overline{u}_{j-1}}{h}(x - x_{j-1})$$

$$P^1_{j,+1}(x) = \overline{u}_{j+1} + \tfrac{\overline{u}_{j+1} - \overline{u}_j}{h}(x - x_{j+1})$$

and a centered parabola:

$$\begin{aligned} P^2_{j,0}(x) \quad &= \quad \overline{u}_j - \tfrac{1}{12}(\overline{u}_{j+1} - 2\overline{u}_j + \overline{u}_{j-1}) + \tfrac{\overline{u}_{j+1} - \overline{u}_{j-1}}{2h}(x - x_j) \\ &\quad + \tfrac{\overline{u}_{j+1} - 2\overline{u}_j + \overline{u}_{j-1}}{h^2}(x - x_j)^2, \end{aligned}$$

where the index n has been suppressed for a simpler notation. The reconstruction $R^2_j(x)$ is a convex combination of the above polynomials:

$$R^2_j(x) = \omega_j^{-1} P^1_{j,-1}(x) + \omega_j^0 P^2_{j,0}(x) + \omega_j^{+1} P^1_{j,+1}(x),$$

with $\omega_j^l \geq 0$ for $l = -1, 0, 1$ and $\sum_l \omega_j^l = 1$. The reconstruction is conservative by construction, i.e.:

$$\frac{1}{h}\int_{x_{j+l}-\frac{h}{2}}^{x_{j+l}+\frac{h}{2}} R_j^2(x)\, dx = \overline{u}_{j+l} \quad \text{for} \quad l = -1, 0, 1.$$

The weights ω_j^l are chosen in order to maximize accuracy on smooth regions, while switching off information coming from non-smooth stencils, when discontinuities are present. The design of the weights follows the strategy proposed in [7]:

$$\omega_j^l = \frac{\alpha_l}{\sum_k \alpha_k} \qquad \alpha_l = \frac{C_l}{(\epsilon + \mathrm{IS}_j^l)^2} \qquad k, l = -1, 0, 1. \tag{3.7}$$

The first term is merely a normalization factor; the C_l's are constants, chosen to maximize accuracy and the IS_j^l are the Smoothness Indicators for the interval I_j, see below. The parameter ϵ prevents division by zero (we always take $\epsilon = 10^{-4}$ in the numerical tests for the Compact CWENO scheme) and diminishes the sensitivity of the scheme to small fluctuations in the Smoothness Indicators, see [12] for the choice of ϵ.

The constants C_l's have been computed in [12]:

$$C_{-1} = \frac{1}{4} \qquad C_0 = \frac{1}{2} \qquad C_{+1} = \frac{1}{4}.$$

The Smoothness Indicators measure the smoothness on I_j of each polynomial involved in the reconstruction. This is achieved estimating a weighted norm of the derivatives of the polynomial. In our case:

$$\begin{aligned} \mathrm{IS}_j^{-1} &= (\overline{u}_j - \overline{u}_{j-1})^2 \\ \mathrm{IS}_j^0 &= \frac{13}{3}(\overline{u}_{j+1} - 2\overline{u}_j + \overline{u}_{j-1})^2 + \frac{1}{4}(\overline{u}_{j+1} - \overline{u}_{j-1})^2 \\ \mathrm{IS}_j^{+1} &= (\overline{u}_{j+1} - \overline{u}_j)^2. \end{aligned} \tag{3.8}$$

This choice ensures that if all IS_j^l are small, $\omega_j^l \simeq C_l$ and the reconstruction is third order accurate in the evaluation of the staggered cell averages. If the grid function $\{\overline{u}_j\}$ is not smooth in $[x_{j-1}, x_{j+1}]$, then only one Smoothness Indicator will be small, and the reconstruction reduces to a one sided straight line. Therefore this scheme degenerates to second order close to discontinuities.

Remark

Usually high resolution schemes are designed to degenerate to first order close to discontinuities in order to develop enough numerical dissipation to control spurious oscillations (see, among others [13] or [14]). The drawback is that accuracy is lost behind shock waves, as pointed out for instance in [4]. The high order Central WENO schemes do not degenerate to first order close to discontinuities and they might generate spurious oscillations at shock collisions, for a very few time steps, since there it is not possible to choose a smooth stencil, because the waves are too close. To assess this point, we have computed the Total Variation as a function of time for the 4th order C-WENO scheme in [11] for a test problem with shock collisions, and we've found no spurious oscillations. On the other hand, accuracy apparently is not lost behind shocks, as our tests on systems [15] seem to suggest.

Note also that this scheme is built on an extremely compact stencil: the third order reconstruction in fact is based on three points.

Once the reconstruction is known, the conservation law is integrated on the staggered control volume $V_{j+1/2}^n$, as in (3.1). To evaluate the integral of the fluxes, as in all staggered central schemes, we use the fact that the numerical solution remains smooth at x_j and x_{j+1}, provided that $\lambda \leq \frac{1}{2}/\max|f'(u)|$. We evaluate the integrals through quadrature. For this scheme we use Simpson's rule in time:

$$\int_{t^n}^{t^{n+1}} f(u(x_j, t))\, dt \simeq \frac{\Delta t}{6}\left[f(u(x_j, t^n)) + 4f(u(x_j, t^n + \frac{\Delta t}{2})) + f(u(x_j, t^n + \Delta t))\right]. \tag{3.9}$$

The first term is computed from the reconstruction. The other terms are evaluated with a second order Runge-Kutta scheme and its corresponding Natural Continuous Extension [20]. Integrating the conservation law in the form $u_t = -\partial_x f(u)$, we have:

$$
\begin{aligned}
u_j^n &= u(x_j, t^n) = R_j^2(x_j) \\
u_j^{n+1/2} &= u\left(x_j, t^n + \tfrac{\Delta t}{2}\right) = u_j^n + \tfrac{\Delta t}{8}(3g_j^1 + g_j^2) \\
u_j^{n+1} &= u\left(x_j, t^n + \Delta t\right) = u_j^n + \tfrac{\Delta t}{2}(g_j^1 + g_j^2),
\end{aligned}
\tag{3.10}
$$

where the g_j's are the Runge-Kutta fluxes of the RK2 scheme. Here, we chose the TVD Heun's scheme, see [16]:

$$
\begin{aligned}
g_j^1 &= -\partial_x f(u^n(x))|_{x_j} \\
g_j^2 &= -\partial_x f\left(u^n(x) + \Delta t g^1(x)\right)|_{x_j}.
\end{aligned}
$$

Note that in order to compute the Runge-Kutta fluxes, it is necessary to interpolate the point values $f(u(x_j, \cdot))$ with a non-oscillatory interpolant and compute its $x-$derivative at each grid point with third order accuracy. This step follows the same lines of the reconstruction we have sketched above. Only, the polynomials P_j's that form the reconstruction now must interpolate the function $f(u(x_j, \cdot))$ in the sense of point values, rather than in the sense of cell averages.

The two one-sided first degree polynomials still have the same form given above. The parabola $P_{j,0}^2$ becomes:

$$
P_{j,0}^2(x) = f_j + \frac{f_{j+1} - f_{j-1}}{2h}(x - x_j) + \frac{f_{j+1} - 2f_j + f_{j-1}}{h^2}(x - x_j)^2,
$$

where $f_j = f(u(x_j, .))$. The weights of the convex combination are kept constant during the whole time step. For more details, see [12]

We use the same discretization to compute the density of cell entropy production on the staggered volume. As for the Nessyahu-Tadmor's scheme we need to compute the reconstruction $R_{j+1/2}^{2,n+1}$ at the end of the time step. We find:

$$
\begin{aligned}
S_{j+1/2}^{W3} = {} & \frac{1}{\Delta t}\left\{ \frac{1}{h}\int_{x_j}^{x_{j+1}} \eta\left(R_{j+1/2}^{2,n+1}(x)\right) - \frac{1}{h}\left[\int_{x_j}^{x_{j+1/2}} \eta\left(R_j^{2,n}(x)\right) + \int_{x_{j+1/2}}^{x_{j+1}} \eta\left(R_{j+1}^{2,n}(x)\right)\right] + \right. \\
& \left. \frac{\lambda}{6}\left[\psi\left(u_{j+1}^n\right) + 4\psi\left(u_{j+1}^{n+1/2}\right) + \psi\left(u_{j+1}^{n+1}\right) - \psi\left(u_j^n\right) - 4\psi\left(u_j^{n+1/2}\right) - \psi\left(u_j^{n+1}\right)\right] \right\}
\end{aligned}
\tag{3.11}
$$

where u_j^n, $u_j^{n+1/2}$ and u_j^{n+1} have already been computed in (3.10).

The numerical results for the entropy production of the Compact CWENO scheme will be discussed in the next section.

3.3 The Central WENO scheme

A complete description of the Central WENO scheme appears in [10].

Here we only outiline the main steps. The reconstruction is, as before, piecewise parabolic:

$$
u^n(x) = \sum_j R_j^2(x)\chi_{I_j}(x).
$$

The parabola $R_j^2(x)$ is assembled using the three parabolas $P_{j-1}(x)$, $P_j(x)$, and $P_{j+1}(x)$, where:

$$
P_j(x) = \overline{u}_j - \frac{1}{24}\left(\overline{u}_{j+1} - 2\overline{u}_j + \overline{u}_{j-1}\right) + \frac{1}{2h}\left(\overline{u}_{j+1} - \overline{u}_{j-1}\right)(x - x_j) + \frac{1}{2h^2}\left(\overline{u}_{j+1} - 2\overline{u}_j + \overline{u}_{j-1}\right)(x - x_j)^2,
$$

and the reconstruction is given by the following convex combination:

$$
R_j^2(x) = \omega_j^{-1}P_{j-1}(x) + \omega_j^0 P_j(x) + \omega_j^{+1}P_{j+1}(x).
\tag{3.12}
$$

Note that the stencil is wider than the stencil we used for the Compact WENO scheme.

The weights ω_j^l are defined as before, see (3.7). The accuracy constants however are different. For the present scheme, the reconstruction from cell averages is fourth order accurate in the evaluation of the staggered space averages provided that: $C^{-1} = C^{+1} = 3/16$, $C^0 = 5/8$. The Smoothness Indicators will be different in this case, because the one-sided polynomials have non-zero second derivatives. More precisely:

$$\begin{aligned}
\mathrm{IS}_j^{-1} &= \tfrac{13}{12}\left(\overline{u}_{j-2} - 2\overline{u}_{j-1} + \overline{u}_j\right)^2 + \tfrac{1}{4}\left(\overline{u}_{j-2} - 4\overline{u}_{j-1} + 3\overline{u}_j\right)^2 \\
\mathrm{IS}_j^{0} &= \tfrac{13}{12}\left(\overline{u}_{j-1} - 2\overline{u}_{j} + \overline{u}_{j+1}\right)^2 + \tfrac{1}{4}\left(\overline{u}_{j+1} - \overline{u}_{j-1}\right)^2 \\
\mathrm{IS}_j^{-1} &= \tfrac{13}{12}\left(\overline{u}_{j} - 2\overline{u}_{j+1} + \overline{u}_{j+2}\right)^2 + \tfrac{1}{4}\left(3\overline{u}_{j} - 4\overline{u}_{j+1} + \overline{u}_{j+2}\right)^2 .
\end{aligned}$$

The parameter ϵ appearing in the definition of the weights (3.7) is always chosen as $\epsilon = 10^{-6}$ for the fourth order scheme. Again, the conservation law is integrated on the staggered control volume $V_{j+1/2}^n$ as in (3.1). The space contribution appearing on the Right Hand Side of (3.1), has a very simple form, which is identical to Nessyahu-Tadmor's case (see § 3.1). Namely:

$$\frac{1}{h}\int_{x_j}^{x_{j+1}} u^n(x)\,dx = \frac{1}{2}\left(\overline{u}_j^n + \overline{u}_{j+1}^n\right) - \frac{h}{8}\left[\left.\frac{dR_{j+1}^2}{dx}\right|_{x_{j+1}} - \left.\frac{dR_j^2}{dx}\right|_{x_j}\right].$$

Simpson's rule is adequate to compute the integral of the fluxes for the fourth order scheme.

We need a more accurate solver than Heun's scheme to evaluate u at the intermediate times $t^n + \frac{\Delta t}{2}$ and $t^n + \Delta t$ in (3.9). Since a RK3 method is not endowed with an accurate enough Natural Continuous Extension, see [20] and [10], we have to upgrade to a more costly RK4 method. Using the standard RK4 scheme (which however is not TVD), we find:

$$\begin{aligned}
u_j^n &= u(x_j, t^n) = R_j^2(x_j) \\
u_j^{n+1/2} &= u\left(x_j, t^n + \tfrac{\Delta t}{2}\right) = u_j^n + \tfrac{\Delta t}{6}\left(\tfrac{5}{4}g_j^1 + g_j^2 + g_j^3 - \tfrac{1}{4}g_j^4\right) \\
u_j^{n+1} &= u\left(x_j, t^n + \Delta t\right) = u_j^n + \tfrac{\Delta t}{6}\left(g_j^1 + 2g_j^2 + 2g_j^3 + g_j^4\right),
\end{aligned} \tag{3.13}$$

where g_j^1, g_j^2, g_j^3 and g_j^4 are the corresponding Runge-Kutta fluxes:

$$\begin{aligned}
g_j^1 &= -\partial_x f(u^n(x))|_{x_j} \\
g_j^2 &= -\partial_x f\left(u^n(x) + \tfrac{\Delta t}{2}\, g^1(x)\right)|_{x_j} \\
g_j^3 &= -\partial_x f\left(u^n(x) + \tfrac{\Delta t}{2}\, g^2(x)\right)|_{x_j} \\
g_j^4 &= -\partial_x f\left(u^n(x) + \Delta t\, g^3(x)\right)|_{x_j}.
\end{aligned}$$

Again, to compute f_x at the intermediate steps of the RK scheme, a reconstruction step is performed. The parabolas P_j's now interpolate the values $f(u_j)$ in the sense of point values. The algorithm is basically the same described in the previous subsection with a few straightforward modifications. The accuracy constants however are different: $C^{-1} = C^{+1} = 1/6$ and $C^0 = 2/3$. In all numerical tests performed here, the Smoothness Indicators were computed only once, at the beginning of the time step.

The entropy production occurring in the control volume $V_{j+1/2}^n$ has the same form of $S_{j+1/2}^{W3}$, (3.11), namely:

$$\begin{aligned}
S_{j+1/2}^{W4} = \frac{1}{\Delta t}\Bigg\{ &\frac{1}{h}\int_{x_j}^{x_{j+1}} \eta\left(R_{j+1/2}^{2,n+1}(x)\right) - \frac{1}{h}\left[\int_{x_j}^{x_{j+1/2}} \eta\left(R_j^{2,n}(x)\right) + \int_{x_{j+1/2}}^{x_{j+1}} \eta\left(R_{j+1}^{2,n}(x)\right)\right] + \\
&\frac{\lambda}{6}\left[\psi\left(u_{j+1}^n\right) + 4\psi\left(u_{j+1}^{n+1/2}\right) + \psi\left(u_{j+1}^{n+1}\right) - \psi\left(u_j^n\right) - 4\psi\left(u_j^{n+1/2}\right) - \psi\left(u_j^{n+1}\right)\right]\Bigg\}
\end{aligned} \tag{3.14}$$

but now $R_j^{2,n}$, $R_{j+1}^{2,n}$ and $R_{j+1/2}^{2,n+1}$ are given by (3.12) and u_j^n, $u_j^{n+1/2}$ and u_j^{n+1} are given by (3.13).

As for the Compact Central WENO scheme, the present method does not degenerate to first order in presence of discontinuities or local extrema.

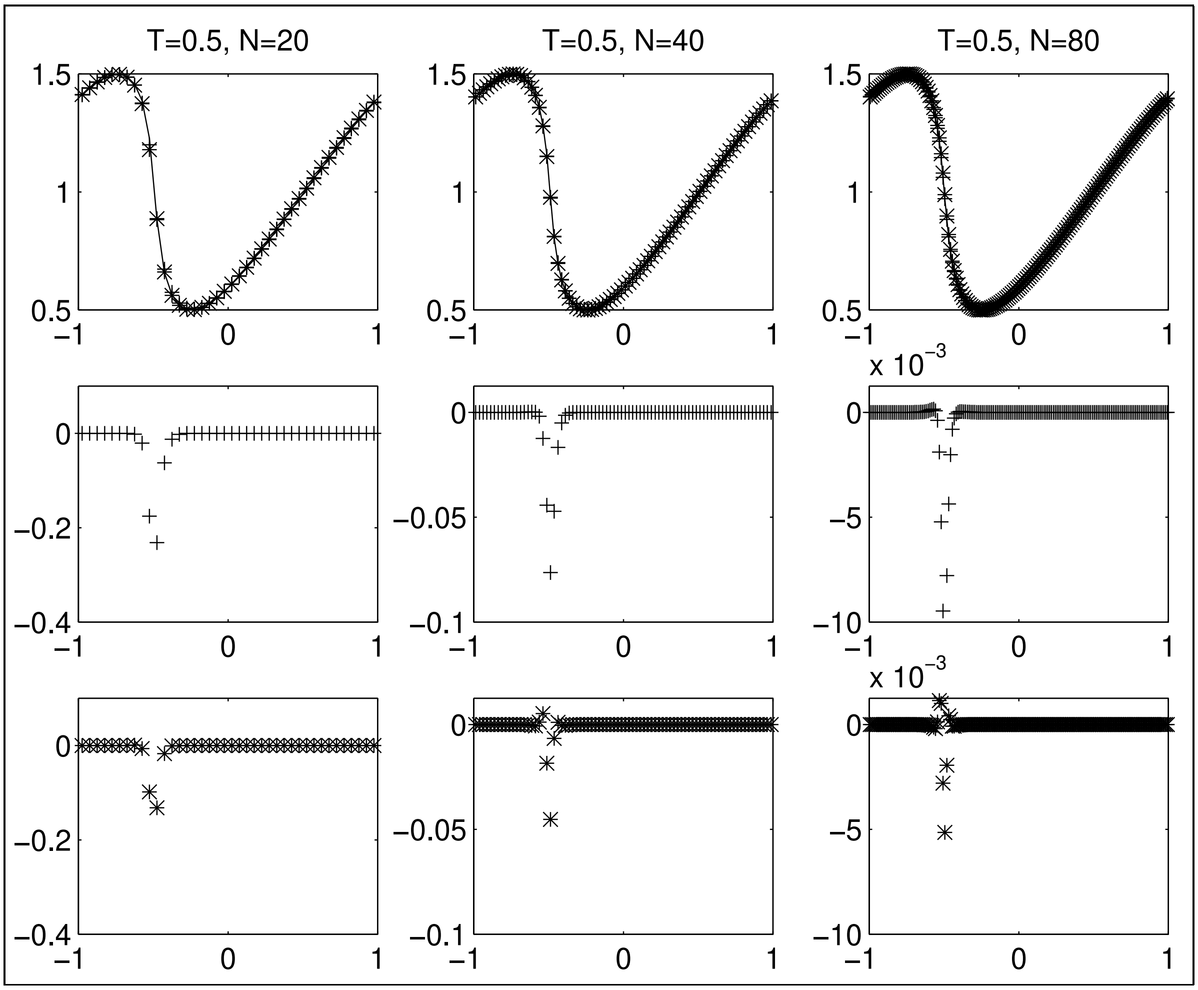

Figure 3.4: Burger's equation. Solution at $T = 0.5$. Entropy production for CCW-3 (second row) and CW-4 (third row) on a smooth flow. $\lambda = 0.66 * 3/7$ for CCW-3, and $\lambda = 0.66 * 2/7$ for CW-4.

The figures in this section show comparisons between the third order Compact Central WENO (CCW-3) scheme, and the fourth order Central WENO (CW-4) scheme.

We use the CFL numbers computed in [2], for the high order Central ENO schemes. The CFL number we will use is 3/7 for CCW-3 and 2/7 for CW-4.

Fig. 3.4 shows the results obtained on Test # 1 at $T = 0.5$, before shock formation. The second and third rows contain the entropy production of the CCW-3 scheme and the CW-4 scheme respectively. The numerical values of the entropy production on the coarsest grids are close to the ones we have already observed in Fig. 2.1 and Fig. 3.1. Here however, the spurious entropy production decreases faster (with the exception of Nessyahu-Tadmor's scheme, with $\theta = 2$, but this changes on finer grids, see Table 4.4). We do expect in fact a fast decay in the spurious entropy production for these higher order schemes.

We note that the entropy production for the CCW-3 and CW-4 schemes has some positive overshoots. The CCW-3 scheme is more diffusive than the CW-4 scheme: in the first case the positive overshoots for the entropy are smaller. On the other hand the more accurate CW-4 scheme has a smaller spurious entropy production than CCW-3.

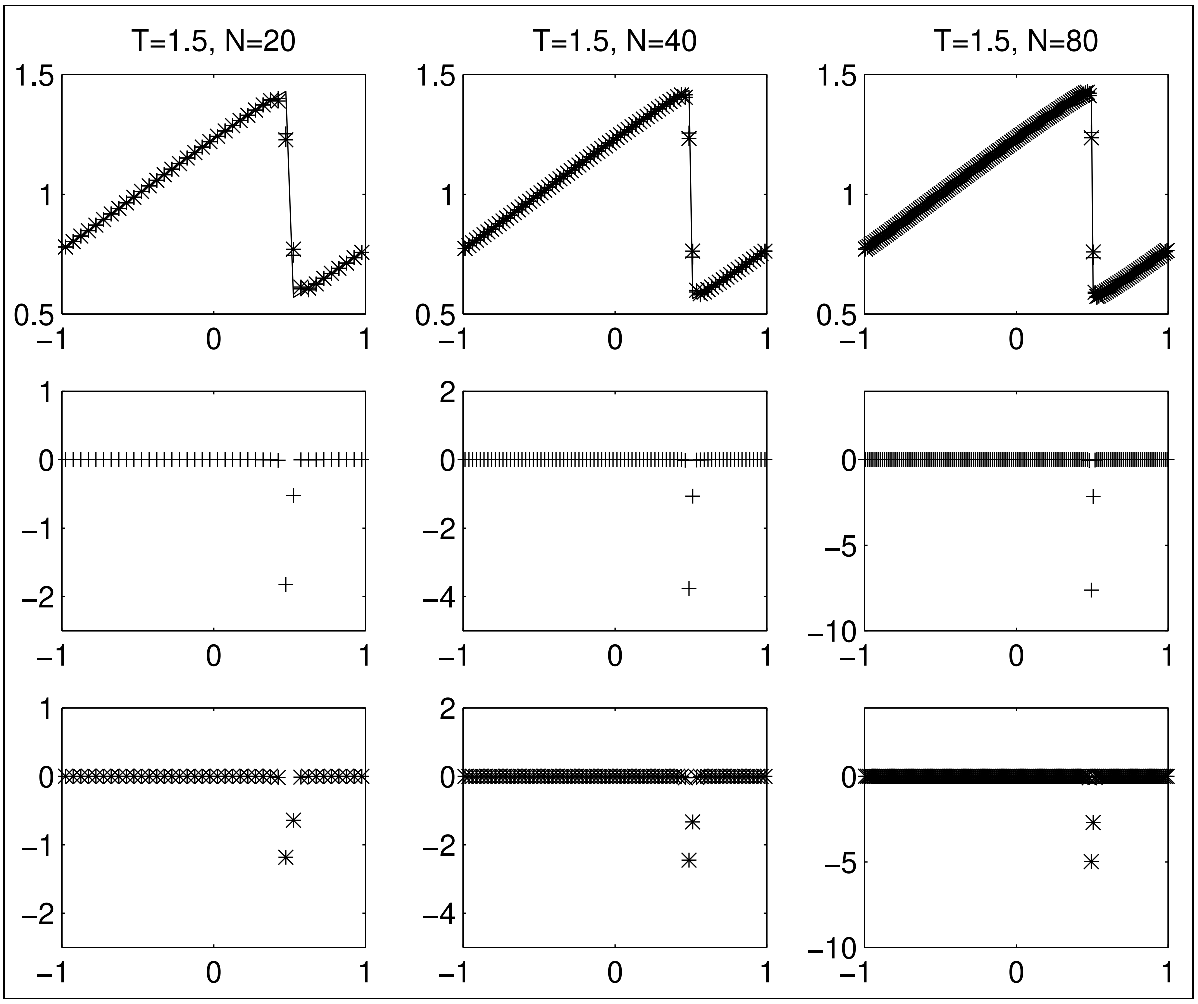

Figure 3.5: Burger's equation. Solution at $T = 1.5$. Entropy production for Compact CWENO-3 (second row) and CWENO-4 (third row) after shock formation. $\lambda = 0.66 * 3/7$ for CCW-3, and $\lambda = 0.66 * 2/7$ for CW-4.

Fig. 3.5 shows the entropy production for the two schemes on a shock wave (Test #1, $T = 1.5$). In both cases, the entropy production goes roughly as $O(1/h)$, as $h \to 0$. The CW-4 scheme has a smaller entropy production than CCW-3.

Finally, Fig. 3.6 shows the results obtained on Test # 2. The first row contains the two numerical solutions. The solution due to the CCW-3 scheme (denoted with +) is slightly more diffusive than the solution due to CW-4. The same behaviour appears in the spurious entropy production, which is slightly larger for CCW-3. The behaviour with respect to grid refinement is different from the lower order schemes: here the peak in the spurious entropy production remains appoximately constant, as the number of grid points is doubled. Therefore the total entropy dissipation on contact discontinuities will go to zero faster than for the lower order schemes, since the transition is spread approximately on the same number of grid points. The entropy production on the angular point decreases much faster than the entropy production on the contact discontinuity, see also §4.2.

4 Applications

In this section we study some applications of the study of the density of entropy production.

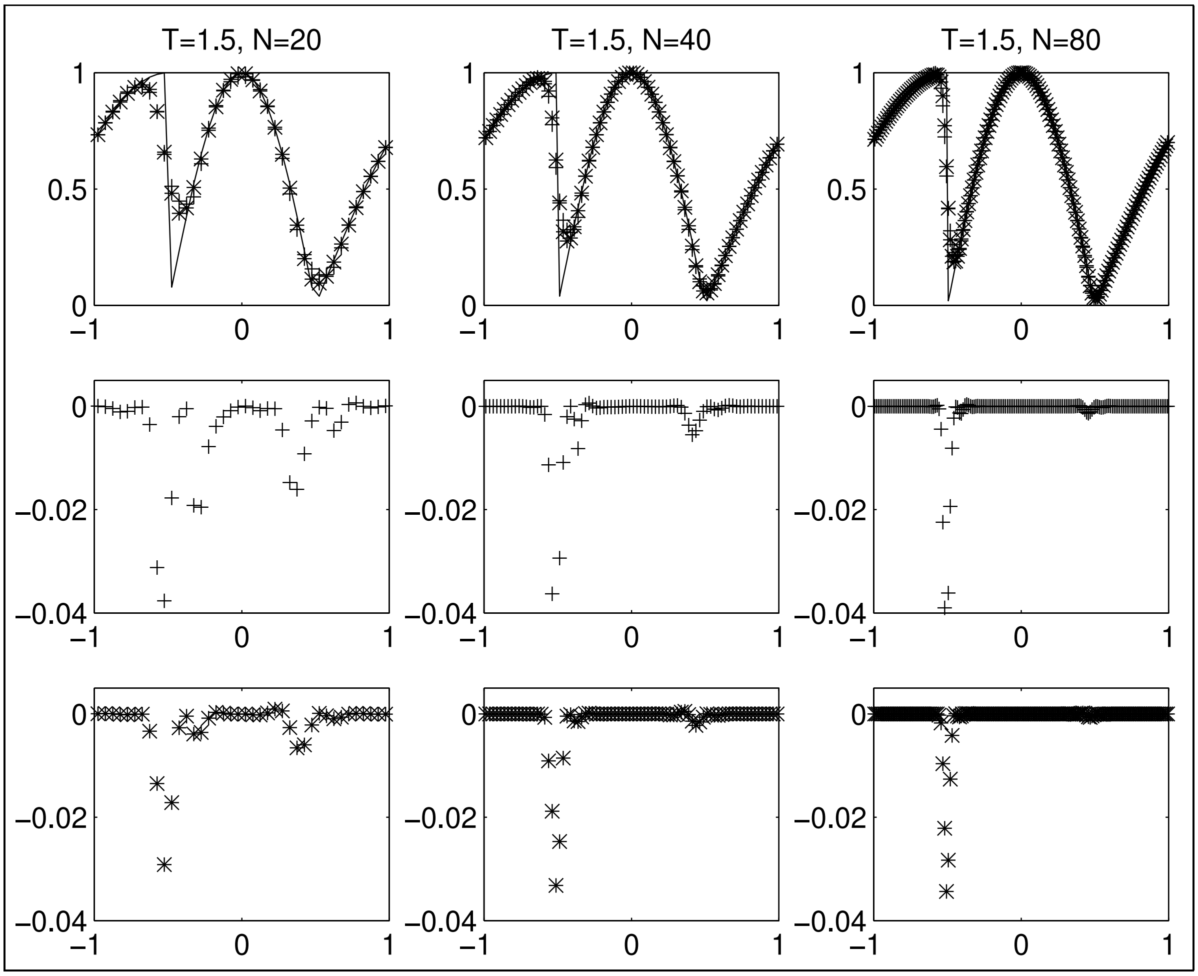

Figure 3.6: Linear advection. Solution at $T = 1.5$. Entropy production for CCW-3 (second row) and CW-4 (third row) on a contact wave. $\lambda = 0.9 * 3/7$ for CCW-3, $\lambda = 0.9 * 2/7$ for CW-4.

We start studying the entropic properties of the CCW-3 and the CW-4 schemes in §4.1. We study the possibility of using the entropy production as a discontinuity detector in §4.2 and as an error indicator in §4.3.

4.1 Are high-order Central WENO schemes entropic?

There are no known results on the entropic properties of high-order schemes (third and higher order). Here we address this important question showing the numerical results obtained on a few test cases. On each test case, we follow the minimum and maximum entropy productions at a fixed time as a function of the grid spacing. These results are shown in Tables 4.1, 4.3 and 4.2 for a smooth flow, a solution with a contact discontinuity and a shocked solution respectively. These solutions are obtained from the test problems of §2.3. The schemes studied are the Compact Central WENO scheme CCW-3 and the fourth order Central WENO, CW-4.

We note that for these tests, the maximum values of the entropy are always positive for both schemes. Therefore these schemes will not be, strictly speaking, entropic.

However it is also apparent that the positive maxima in the entropy production are always much smaller then the minima (in absolute value). On the smooth transition, Table 4.1, the positive overshoots converge to zero, as the grid is refined, for both schemes, although this behaviour can be observed

Maximum and minimum entropy production
on a smooth transition

	CCW-3		CW-4	
	min	max	min	max
N = 10	-.61582	.155e-3	-.44818	.381e-4
N = 20	-.23138	.938e-4	-.13171	.963e-3
N = 40	-.07630	.224e-3	-.04519	.521e-2
N = 80	-.01071	.158e-3	-.00514	.114e-2
N = 160	-.00158	.710e-4	-.28e-3	.114e-3
N = 320	-.20e-3	.185e-4	-.11e-4	.707e-5

Table 4.1: Burger's equation, $T = 0.5$, $\lambda = 0.66 * 3/7$ for CCW-3, $\lambda = 0.66 * 2/7$ for CW-4.

only beyond a certain value of N. For the CCW-3 scheme, the positive overshoots do not seem to convergence to zero when a discontinuity occurs, see Tables 4.2 and 4.3. Note however, that the amplitude of the positive overshoots is orders of magnitude smaller than the minima in the entropy production.

The situation is particularly clear in Table 4.1. Here the entropy production is spurious, because the flow is smooth. Both the negative and positive overshoots converge to zero (in §4.3 we will see that the rate of convergence is approximately equal to the accuracy of the scheme). The positive overshoots are always smaller than the minimum values, especially on coarse grids, where the error is larger.

Maximum and minimum entropy production
on a solution with a shock

	CCW-3		CW-4	
	min	max	min	max
N = 10	-0.7795	.661e-3	-0.5458	.266e-3
N = 20	-1.8230	.458e-3	-1.1817	.954e-4
N = 40	-3.7608	.267e-3	-2.4491	.246e-3
N = 80	-7.6189	.214e-3	-4.9821	.417e-4
N = 160	-15.326	.595e-3	-10.046	.304e-4
N = 320	-30.736	.200e-2	-20.167	.268e-4

Table 4.2: Burger's equation, $T = 1.5$, $\lambda = 0.66 * 3/7$ for CCW-3; $\lambda = 0.66 * 2/7$ for CW-4. The minima always occur in cells containing the shock

When a shock occours, see Table 4.2, the minimum values for the entropy production increase, in absolute value, with respect to grid refinement, as $O(\frac{1}{h})$. The positive overshoots still decrease to zero for the CW-4 scheme. For the CCW-3 scheme, the positive overshoots decrease as the grid is refined on coarse grids, but this behaviour is reversed on finer grids. The situation is similar on contacts, Table 4.3. Here the positive overshoots are still smaller than the spurious negative minima of entropy production. While the spurious minima remain approximately constant under grid refinement, the positive overshoots go to zero, at least in the case of the CW-4 scheme.

The analysis of these data suggests that it will not be possible to prove that these high-order schemes are entropic. However, we conjecture that at least the CW-4 scheme might be Essentially Entropic in the sense that positive overshoots in the values of the cell entropy prodution are possible, but their amplitude decreases as the grid is refined.

Maximum and minimum entropy production
on a solution with a contact wave

	CCW-3		CW-4	
	min	max	min	max
N = 10	-.04685	.184e-4	-.02015	.530e-3
N = 20	-.03765	.656e-3	-.02913	.909e-3
N = 40	-.04590	.613e-3	-.03316	.481e-3
N = 80	-.04901	.356e-3	-.03432	.194e-3
N = 160	-.04725	.367e-3	-.03409	.664e-4
N = 320	-.04413	.631e-3	-.03336	.215e-4

Table 4.3: Linear advection, $T = 1.5$, $\lambda = 0.9 * 3/7$ for CCW-3; $\lambda = 0.9 * 2/7$ for CW-4. The minima always occur in cells containing the contact wave

4.2 Entropy production as a discontinuity detector

We study quantitatively the data in the density of entropy production on different transitions, to see whether it is possible to use the entropy production to automatically classify discontinuities. This information can be applied in several ways.

It is important in a strategy of grid adaptivity, to select the regions where a shock occurs to prevent the crowding of too many grid points close to the discontinuity. High order schemes are able in fact to resolve well a shock wave even on a coarse grid (see for instance Fig. 3.2 or Fig. 3.5).

It can also be useful to be able to select the regions containing contact discontinuities. These transitions in fact are poorly resolved even by high order schemes (see Fig 3.6). Algorithms acting as slope correctors are available to improve the resolution of contact discontinuities, as the Artificial Compression Method of [19]. These slope correctors tipically artificially increase the slope of characteristics, transforming contact waves into shocks. They are not entropic, so it is advisable to apply them only on discontinuities, to prevent the occurrence of expansion shocks.

To study the behaviour of the entropy production as a singularity detector, we consider again a smooth flow (Test #1 of § 2.3 at $T = 0.5$), a solution with a shock (again Test #1, at $T = 1.5$), and a contact discontinuity (Test # 2 of § 2.3, at $T = 1.5$).

For all schemes considered, we compute the minimum value of the entropy production as a function of the grid. The minimum in the entropy production occurs always in the cells crossed by the shock, in Test #1 at $T = 1.5$, or in the cells on which the contact discontinuity is spread in Test #2.

Minimum density of entropy production
on a smooth transition

	$N = 10$	$N = 20$	$N = 40$	$N = 80$	$N = 160$	$N = 320$
Lax-Friedrichs	-.39291	-.35771	-.26949	-.17934	-.11246	-.06331
Godunov	-.30017	-.32159	-.22080	-.14193	-.08873	-.04967
NT, $\theta = 1$	-.35916	-.27751	-.10578	-.02330	-.00614	-.00151
NT, $\theta = 2$	-.19799	-.12259	-.02220	-.00209	-.00023	-.70e-4
CCW-3	-.61582	-.23138	-.07630	-.01071	-.00158	-.20e-3
CW-4	-.44818	-.13171	-.04519	-.00514	-.28e-3	-.11e-4

Table 4.4: Burger's equation before shock formation at $T = 0.5$. The NT and Lax Friedrichs scheme have $\lambda = 0.33$; $\lambda = 0.66$ for Godunov scheme; $\lambda = 0.66 * 3/7$ for CCW-3, $\lambda = 0.66 * 2/7$ for CW-4.

The results are contained in Table 4.4, Table 4.5 and Table 4.6. Table 4.4 shows the minima of the density of entropy production occurring on a smooth flow. For the central schemes, the CFL is

$\lambda \le \frac{1}{2} \cdot \frac{2}{3}$, since $\max|f'(u)| = \frac{3}{2}$ for Test #1. The Lax Friedrichs and Nessyahu-Tadmor's schemes have $\lambda = 0.33$. Godunov scheme has $\lambda = 0.66$. The higher order CCW-3 and CW-4 have a stricter CFL restriction, [2]: here we used $\lambda = 0.66 \cdot \frac{3}{7}$ for the CCW-3 scheme and $\lambda = 0.66 \cdot \frac{2}{7}$ for the CW-4 scheme.

The entropy production is spurious in this test problem and we note that the amplitude of the minima decrease approximately as $O(h)^r$, where r is the accuracy of the scheme. We report the actual order in Table 4.7.

Minimum density of entropy production on a shock

	$N = 10$	$N = 20$	$N = 40$	$N = 80$	$N = 160$	$N = 320$
Lax-Friedrichs	-0.4080	-1.0429	-2.2093	-4.5666	-9.2760	-18.717
Godunov	-0.4401	-1.0337	-2.1704	-4.4568	-9.0288	-18.178
NT, $\theta = 1$	-0.7859	-1.9356	-4.1181	-8.4142	-17.049	-34.357
NT, $\theta = 2$	-0.7054	-1.7199	-3.4398	-6.9112	-13.856	-27.864
CCW-3	-0.7795	-1.8230	-3.7608	-7.6189	-15.326	-30.736
CW-4	-0.5458	-1.1817	-2.4491	-4.9821	-10.046	-20.167

Table 4.5: Burger's equation after shock formation at $T = 1.5$. The NT and Lax Friedrichs schemes have $\lambda = 0.33$; $\lambda = 0.66$ for Godunov scheme; $\lambda = 0.66 * 3/7$ for CCW-3, $\lambda = 0.66 * 2/7$ for CW-4. The minima are always located on the shock.

The entropy production on a shock is shown in Table 4.5. We immediately see that on shocks the entropy approximately doubles as the mesh width is halved, for all schemes studied. Moreover, the number of grid points on which the shock is spread is independent of h, see Figures 2.2, 3.2 and 3.5. Therefore the total entropy dissipated on the shock

$$\mathcal{S} = \sum_j S_j h \to \text{const} \qquad \text{as} \quad h \to 0,$$

where the sum is extended to the cells on which the shock is spread. Comparing Table 4.4 and Table 4.5 we clearly see that the density of entropy production on the smooth transition is orders of magnitude smaller (in absolute value) than the entropy dissipated on the shock, expecially on fine grids and for the higher order schemes. Moreover, from Fig. 2.2, Fig. 3.2 and Fig. 3.5, we note that the cells containing the shock are characterized by very sharp and isolated peaks in the entropy production. Therefore shocks seem to be easily identified. We conclude that an indicator based on the density of entropy production can be easily built to single out those cells crossed by a shock.

Minimum density of entropy production
on a contact discontinuity

	$N = 10$	$N = 20$	$N = 40$	$N = 80$	$N = 160$	$N = 320$
Lax-Friedrichs	-.04432	-.04659	-.05887	-.07223	-.08111	-.08826
Godunov	-.04359	-.04818	-.06036	-.07324	-.08186	-.08878
NT, $\theta = 1$	-.03645	-.05079	-.04943	-.07533	-.09773	-.11441
NT, $\theta = 2$	-.03057	-.03815	-.03791	-.06384	-.10890	-.11381
CCW-3	-.04685	-.03765	-.04590	-.04901	-.04725	-.04413
CW-4	-.02015	-.02913	-.03316	-.03432	-.03401	-.03336

Table 4.6: Linear advection at $T = 1.5$. The NT and Lax Friedrichs schemes have $\lambda = 0.45$; $\lambda = 0.9$ for Godunov scheme; $\lambda = 0.9 * 3/7$ for CCW-3, $\lambda = 0.9 * 2/7$ for CW-4. The minima are located in the cells containing the contact wave.

The results obtained on the contact wave appear in Table 4.6. Here $\lambda = 0.45$ for the Lax Friedrichs and Nessyahu-Tadmor's schemes; $\lambda = 0.9$ for Godunov scheme, while $\lambda = 0.9 \cdot \frac{3}{7}$ for CCW-3 and $\lambda = 0.9 \cdot \frac{2}{7}$ for the CW-4 scheme.

For the lower order schemes the entropy production slowly increases as the grid is refined, but the increase is much slower than in the case of shocks. For the CCW-3 and the CW-4 schemes the density of entropy production is approximately constant, with respect to the number of grid points. Therefore the total entropy $\mathcal{S}$ produced on the contact wave goes to zero, as $h \to 0$, for all schemes studied.

It is more difficult to identify cells containing contact discontinuities, than cells containing shocks. From the data we have gathered, it seems that this task requires first to isolate those cells where the entropy production is large enough to contain a possible discontinuity. On these cells, one should compute the entropy production with two different grids, say h and $h/2$, and classify the transition according to the behaviour observed on the dependence on h of the cell entropy production.

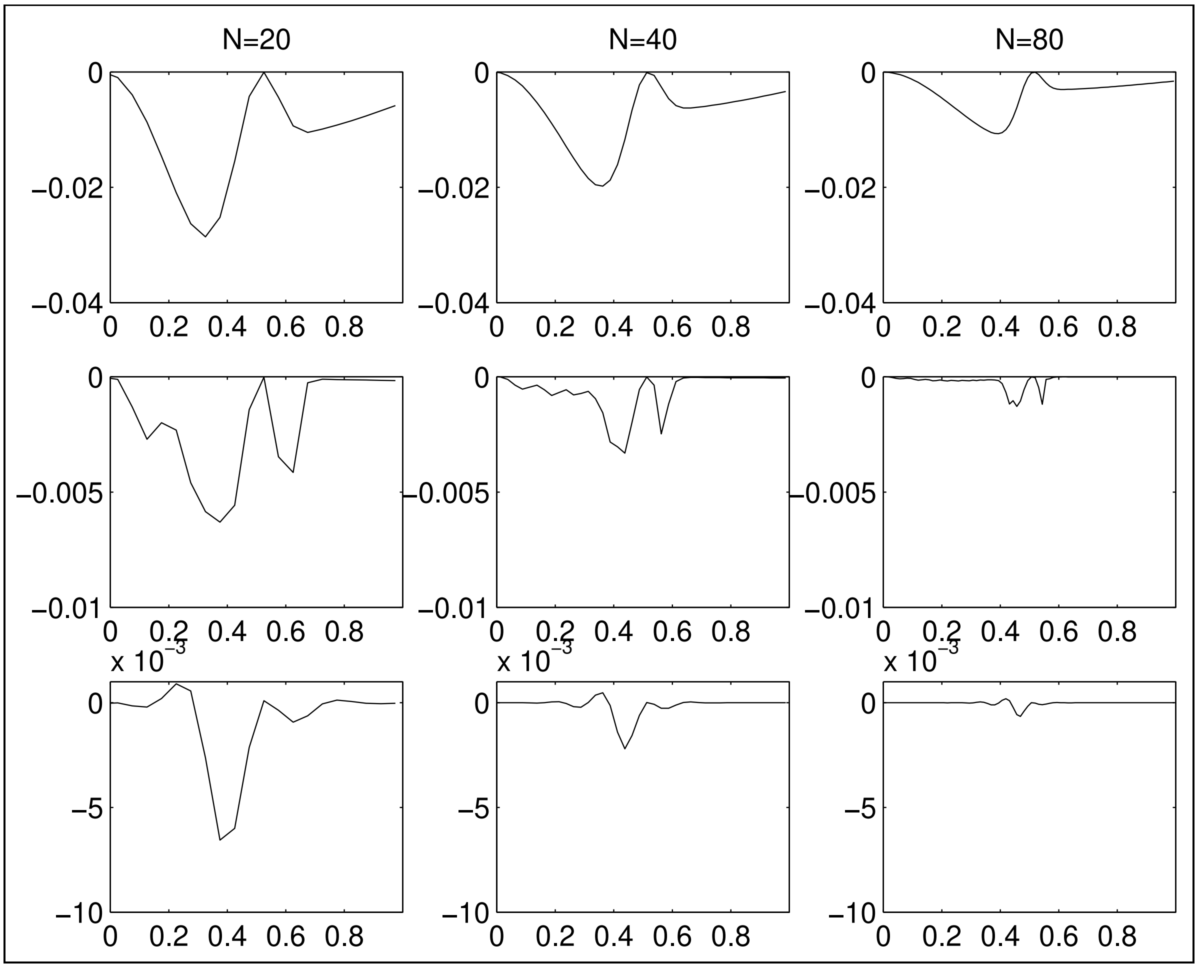

Figure 4.1: Linear equation. Solution at $T = 1.5$. Entropy production on the angular point for Lax Friedrichs scheme (first row), Nessyahu-Tadmor's scheme (second row) and CW-4 (third row)

We end this section discussing the behaviour of the density of entropy production on a non smooth transition, such as the angular point of Test #2 of §2.3.

Fig. 4.1 is a zoom of the figures abtained with Test #2 for Lax Friedrichs, Nessyahu-Tadmor's scheme with $\theta = 1$, and CW-4. Here only the values with $x \in [0, 1]$ are shown.

The density of entropy production is largest immediately before and after the angular point (compare with Figures 2.3, 3.3, 3.6, where the numerical solution is also shown).

We note that for the first order scheme the density of entropy production on the angular point in absolute value decreases roughly as $O(h)$. The first order schemes therefore do not recognize this singularity, as is to be expected. The higher order schemes are more selective: the density of entropy production (in absolute value) on the angular point decreases faster than in the presence of the contact discontinuity, but slower than in the case of smooth flow.

4.3 Entropy production as error indicator

In Table 4.7 we show the order with which the minima in the spurious entropy production of Table 4.4 go to zero, as the grid is refined.

Rate of convergence for entropy production on a smooth transition

	$N=10$	$N=20$	$N=40$	$N=80$	$N=160$
Lax-Friedrichs	0.06	0.41	0.59	0.67	0.83
Godunov	-0.10	0.54	0.64	0.68	0.83
NT, $\theta=1$	0.37	1.39	2.18	1.93	2.02
NT, $\theta=2$	0.69	2.47	3.40	3.19	1.71
CCW-3	1.42	1.60	2.83	2.76	3.01
CW-4	1.76	1.55	3.14	4.18	4.66

Table 4.7: Burger's equation before shock formation at $T=0.5$. The NT and Lax Friedrichs schemes have $\lambda=0.33$; $\lambda=0.66$ for Godunov scheme; $\lambda=0.66*3/7$ for CCW-3, $\lambda=0.66*2/7$ for CW-4.

Each column of Table 4.7 contains the values of $\log_2(\min(S_{j,h})/\min(S_{j,h/2}))$. We note that on average $\min(S_{j,h}) \to 0$ as $O(h)^r$, where r is the accuracy of the scheme. For the first order schemes, the rate of convergence here appears to be slower than h. This improves if we choose a smoother solution. For example, if we sample the data for the Lax Friedrichs scheme at $T=0.3$ instead of $T=0.5$, then the rate with which $S_j^{LF} \to 0$ is indeed first order. The problem here is that at $T=0.5$, the Lax Friedrichs scheme does not "see" the transition as smooth on coarse grids. The relatively high entropy values encountered in some cells indeed label those cells as not being small enough to resolve the transition.

These data suggest that the spurious entropy production on smooth flows goes to zero with the same rate of the local truncation error.

To compare the local behaviour of the error and the entropy production, we consider again Test #1 at T=0.5.

Fig. 4.2 shows a comparison between the actual error (third row) and the entropy production (second row) for the CW-4 scheme on Burger's equation, before shock formation. We see that the entropy production indeed peaks where the error is largest, and both quantities have a similar behaviour. Moreover the amplitude and the width of the peaks in the error and in the entropy production undergo the same changes under grid refinement.

In Fig. 4.3, the same test problem has been applied to Nessyahu-Tadmor's scheme, with the MinMod limiter ($\theta=1$). Here we note that the error has two main contributions: where the transition is steep, the error is due to a lack of resolution in the grid. This phenomenon is caught also by the entropy production, which has a peak in this region. Another source of error is due to the clipping phenomenon characteristic of the MinMod limiter, in the presence of local extrema. This phenomenon is responsible for the secondary peaks that appear in the plots of the error. This source of error unfortunately is not detected by the entropy production. The entropy production in fact is very small in regions where the numerical solution is approximately constant, and therefore is not able to detect this type of error. Note that even error indicators based on the local derivatives of the numerical solution would not detect the need for grid refinement in these regions.

Another example is in Fig. 4.4. The test problem is the same as before, i.e. Burger's equation before shock formation, with the third order CCW-3 scheme. In the first two columns, we have $\lambda=0.77*3/7$.

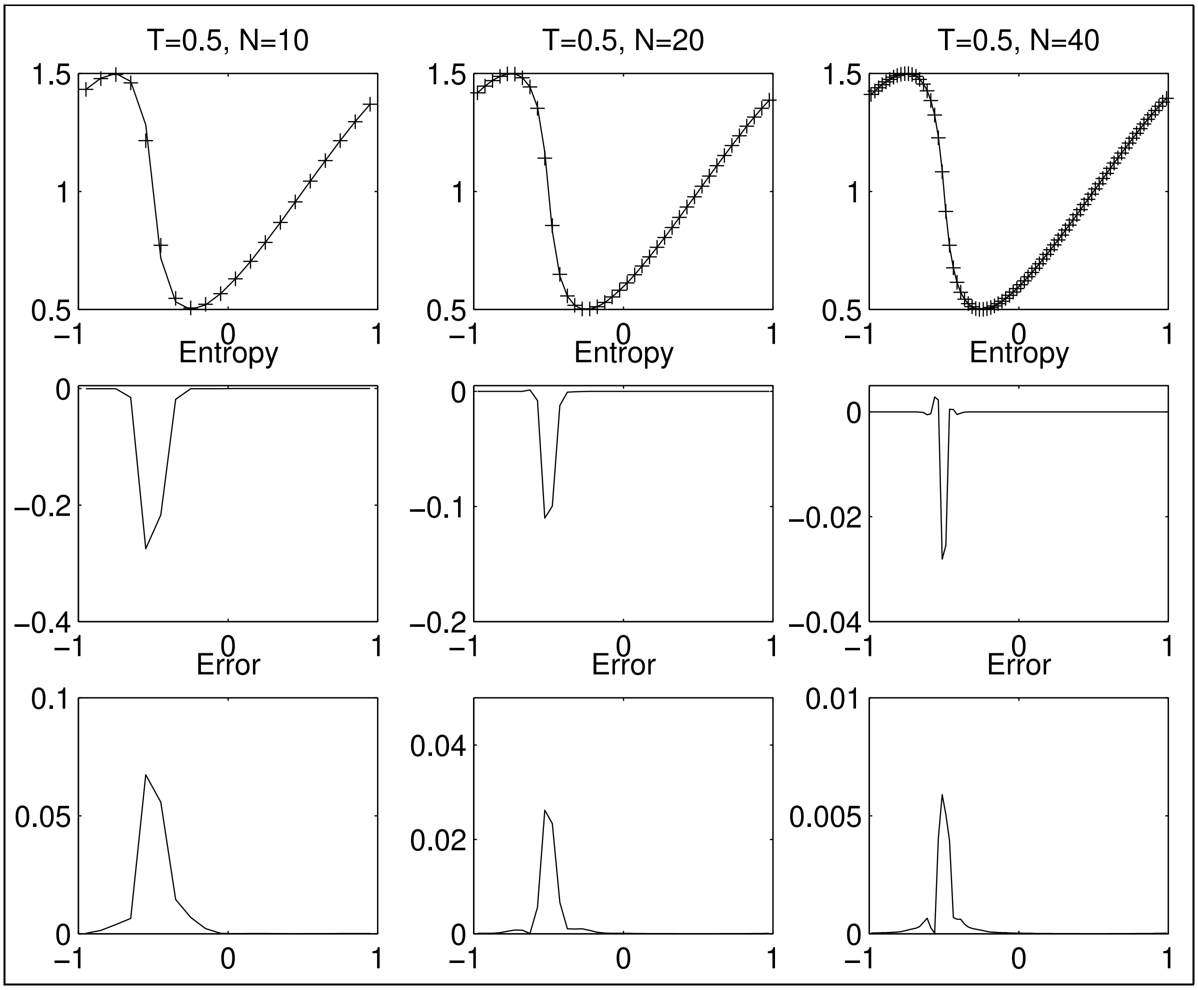

Figure 4.2: Burger's equation. Solution at $T = 0.5$. Entropy production for the CW-4 scheme (second row) and error (third row) on a smooth wave, $\lambda = 0.66 * 2/7$

This is slightly above the actual CFL for this scheme, which, for this problem, is $\lambda = 0.66 * 3/7$. For $N = 80$ (left column) the solution is stable, and both the entropy and the error have a similar behaviour. In the second column, with $N = 160$, the numerical solution is slightly unstable. Small wiggles appear in the maximum of the solution, although they are barely visible on this scale. These of course are reflected on the error, which however is still small. Interestingly, the entropy reacts to these unphysical oscillations with a region of positive entropy production that signals not only that the error is larger here than in the neighboring cells, but it also shows that something is wrong in the numerical solution.

As λ is decreased (third column), the wiggles disappear, together with the region of positive entropy production.

Therefore the magnitude of the density of entropy production mimics the behaviour of the error, and in this sense, it can be used as an a posteriori error indicator for grid adaptivity.

Moreover, we can also use the sign of the entropy production to signal the need for more dissipation. We can achieve this goal by decreasing the mesh ratio λ or by switching to a lower order scheme.

These results are very preliminary and they require further investigation. We study the case of systems of equations in [15]. To effectively use the entropy production as an error indicator, it is important to be able to estimate constants c_1 and c_2 such that:

$$c_1|S_j| \leq |e_j| \leq c_2|S_j|,$$

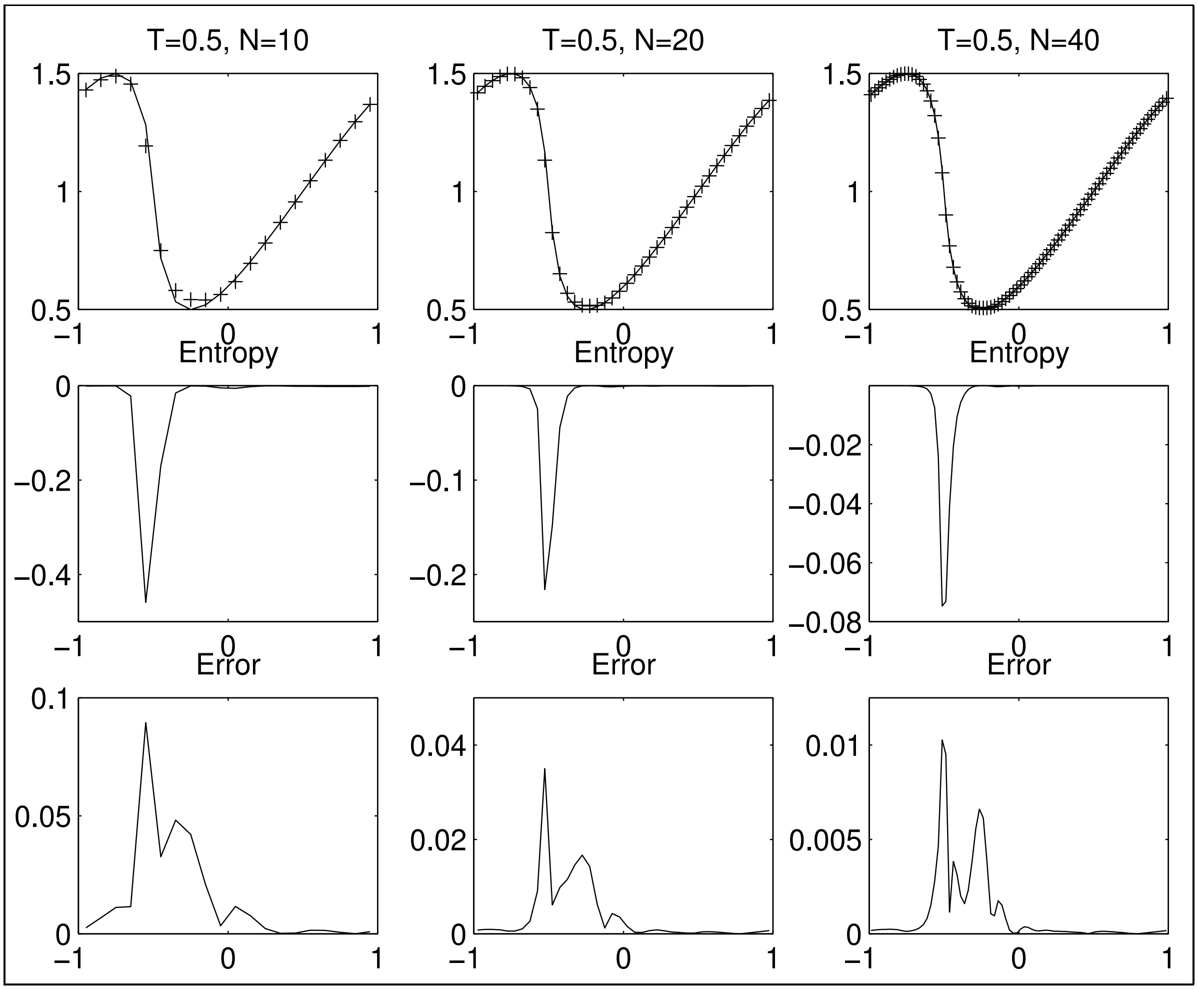

Figure 4.3: Burger's equation. Solution at $T = 0.5$. Entropy production for the Nessyahu-Tadmor's scheme (second row) and error (third row) on a smooth wave, $\lambda = 0.33$, $\theta = 1$.

where e_j is the local error. These constants are clearly problem dependent, and they will also depend on the particular scheme being chosen. However, the difficulties inherent in the nonlinearity of conservation laws and high order non-oscillatory schemes make it unlikely that c_1 and c_2 can be actually analitically computed. Again, the experience gained from numerical tests becomes essential to devise a sound strategy for the design of the error indicator.

References

[1] Andrews J.G., Morton K.W., *A Posteriori Error Estimation Based on Discrepancies in an Entropy Variable*, IJCFD, **10**, (1998), 183-198.

[2] Bianco F., Puppo G., Russo G., *High Order Central Schemes for Hyperbolic Systems of Conservation Laws*, International Series of Numerical Mathematics, v. 129, Birkhauser Verlag, 1999, 55-64.

[3] Bouchut F., Bourdarias Ch., Perthame E. B., *A MUSCL Method Satisfying All the Numerical Entropy Inequalities*, Math. Comp., **65**, No. 216, (1996), 1439-1461.

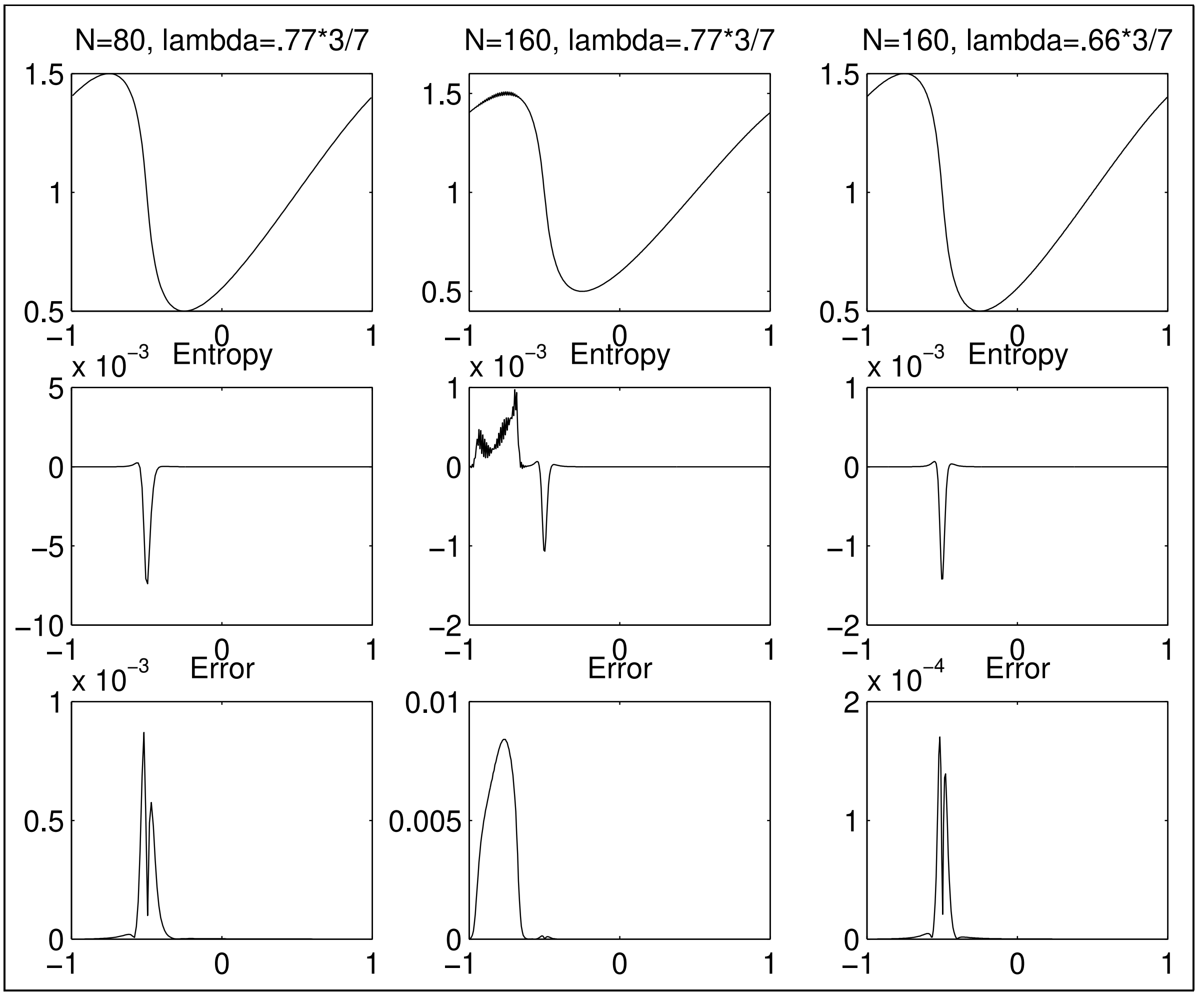

Figure 4.4: Burger's equation. Solution at $T = 0.5$. Entropy production for the third order CCW-3 scheme (second row) and error (third row) on a smooth wave.

[4] Casper J., Carpenter M.H. *Computational Consideration for the Simulation of Shock Induced Sound*, SIAM J. Sci. Comp., v. 19, No. 3, (1998), 813-828.

[5] Cockburn B., Shu C.W., *TVB Runge-Kutta Local Projection Discontinuous Galerkin Finite Element Method for Conservation Laws II: General Framework*, Math. Comp., **52**, No. 186, (1989), 411-435.

[6] Godlewski E., Raviart P.-A., *Numerical Approximation of Hyperbolic Systems of Conservation Laws*, Springer, New York, 1996.

[7] Jiang G.-S., Shu C.-W., *Efficient Implementation of Weighted ENO Schemes*, JCP, **126**, (1996), 202-228.

[8] Kruzkov S. N., *First Order Quasilinear Equations in Several Independent Variables*, Math. USSR Sb 10, (1970), 217-243.

[9] LeVeque R. J., *Numerical Methods for Conservation Laws*, Lectures in Mathematics, Birkhauser Verlag, Basel, 1992.

[10] Levy D., Puppo G., Russo G., *Central WENO Schemes for Hyperbolic Systems of Conservation Laws*, Math. Model. and Numer. Anal., **33**, No. 3 (1999), 547-571.

[11] Levy D., Puppo G., Russo G., *On the Behavior of the Total Variation in CWENO Methods for Conservation Laws*, Proceedings ICOSAHOM '98, Appl. Nume. Math., **33**, (2000), 415-421.

[12] Levy D., Puppo G., Russo G., *Compact Central WENO Schemes for Multidimensional Conservation Laws*, SIAM J. Sci. Comp., **22**, 2000, No. 2, 656-672.

[13] Liu X.D., Osher S., *Convex ENO High Order Multidimensional Schemes without Field by Field Decomposition or Staggered Grids*, JCP, **142**, No. 2 (1998), 304-330.

[14] Nessyahu H., Tadmor E., *Non-oscillatory Central Differencing for Hyperbolic Conservation Laws*, JCP, **87**, No. 2 (1990), 408-463.

[15] Puppo G., *Numerical Entropy Production for Central Schemes: Systems of Equations*, in preparation.

[16] Shu C.W., Osher S., *Efficient Implementation of Essentially Non-Oscillatory Shock Capturing Schemes*, JCP, v. 77, (1988), 439-471.

[17] Sonar T., Süli E., *A Dual Graph Norm Refinement Indicator for Finite Volume Approximations of the Euler Equations*, Numer. Math., **78**, (1998), 619-658.

[18] Tadmor E., *Approximate Solutions of Nonlinear Conservation Laws*, in Advanced Numerical Approximation of Nonlinear Hyperbolic Equations, Lecture Notes in Mathematics (editor: A. Quarteroni), Springer, Berlin, 1998.

[19] Yang H., *An Artificial Compression Method for ENO schemes, the Slope Modification Method*, JCP, No. 89, (1990), 125-160.

[20] Zennaro M., *Natural Continuous Extensions of Runge-Kutta Methods*, Math. Comp., **46**, (1986), 119-133.